Angular Dependence of the Relative Photon Detection Efficiency of Silicon Photomultipliers

von

Daniel Wilson

Bachelorarbeit in Physik

vorgelegt der
Fakultät für Mathematik, Informatik und Naturwissenschaften
der
Rheinisch-Westfälischen Technischen Hochschule Aachen

Vorgelegt im September 2012

angefertigt am

III. Physikalischen Institut A

Erstgutachter und Betreuer

Prof. Dr. Thomas Hebbeker
III. Physikalisches Institut A
RWTH Aachen

Zweitgutachter

Prof. Dr. Christopher Wiebusch
III. Physikalisches Institut B
RWTH Aachen

Abstract

FAMOUS[1] is a prototype for a silicon photomultiplier (SiPM) based fluorescence telescope, which uses Winston cones as light funnels. These Winston cones are non imaging devices with a wide range of exit angles, which are used to concentrate the incoming light on a system of silicon photomultipliers to detect the fluorescence light of extensive air showers.

For this reason, the angular dependence of the relative photon detection efficiency of silicon photomultipliers is studied in this thesis. For the measurement of the relative photon detection efficiency, a measurement setup was designed which makes fully automatic measurements possible. Throughout this thesis, measurements for 5 different wavelengths and two SiPMs in different orientations have been performed. It has been shown that the relative photon detection efficiency lies above 90% up to incident angles of 75° for wavelengths from the UV range (371 nm) to red light (630 nm). The measured data fits well to the theory given by a Monte Carlo simulation using the Fresnel equations. This Monte Carlo simulation takes multiple reflections between the silicon and the resin, which is covering the silicon protecting it from mechanical damage, into account.

Zusammenfassung

FAMOUS[1] ist ein Prototyp für ein Fluoreszenzteleskop, welches auf Silizium-Photomultipliern (SiPM) basiert und Winston Kegel als Lichttrichter nutzt. Diese Winston Kegel sind nicht abbildende optische Elemente, die eine breite Verteilung von Austrittswinkeln aufweisen und dazu benutzt werden, das Fluoreszenzlicht von teilcheninduzierten Luftschauern auf das System von Silizium-Photomultipliern zu konzentrieren.

Aus diesem Grund ist die Winkelabhängigkeit der relativen Photondetektionseffizienz in dieser Arbeit untersucht worden. Für die Messungen wurde ein Messaufbau entwickelt, der eine vollautomatische Messung ermöglicht. In dieser Arbeit wurden Messungen für fünf verschiedene Wellenlängen und zwei verschiedene SiPMs in verschiedenen Orientierungen durchgeführt. Dadurch konnte gezeigt werden, dass die relative Photodetektionseffizienz für verschiedene Wellenlängen, vom UV-Bereich (371 nm) bis zum roten Licht (630 nm), über 90% bis zu einem Einfallswinkel von 75° beträgt. Die gemessenen Daten passen gut zu der Theorie, die durch eine Monte-Carlo-Simulation gegeben ist, welche auf den Fresnel Gleichungen beruht. Diese Monte-Carlo-Simulation berücksichtigt, dass es zu Vielfachreflektionen zwischen dem Silizium und dem Harz, welches das Silizium vor Beschädigungen schützt, kommen kann.

[1] FAMOUS - First Auger Multi pixel photon counter camera for the Observation of Ultra-high-energy cosmic ray Showers

Contents

List of Figures

1. Introduction

One century ago, Victor F. Hess undertook his balloon flights at altitudes up to 5 km that won him the Nobel prize in 1936. Up this point, scientists believed that the source of ionizing radiation was the crust of Earth, but Hess found an increase of ionizing radiation with higher distance from Earth. At 5 km altitude, the radiation was twice as high as it was on sea level, thus he concluded that the origin of this radiation must be the cosmos.

These days, there are still many questions open depending cosmic rays. Most cosmic rays have energies between 10 MeV and 10 GeV, but there are also cosmic rays which have been accelerated to energies up to 10^{20} eV. The flux of the radiation decreases steeply with the energy to one particle per century and square kilometre at energies above 100 EeV[1]. Cosmic rays with an energy above 10^{18} eV are called ultra-high-energy cosmic rays (UHECR). It is unknown, which sources are capable of accelerating these particles up to such high energies, much higher energies than achieved at the Large Hadron Collider (LHC).

For this reason, these particles are studied at several cosmic-ray observatories all over the world. One of them is the Pierre Auger Observatory in Argentina. Besides the surface detector, consisting of 1660 water Cherenkov detectors distributed over an area of 3000 km^2, there are 27 fluorescence detectors which detect the fluorescence light generated by incoming particles due to excitation of nitrogen in our atmosphere. The advantage of this technique is the minimal reliance on the shower models, but obviously, the telescope can only be operated during moonless nights.

At the moment, photomultiplier tubes (PMTs) are embedded in the cameras of the fluorescence detectors to detect the ultraviolet fluorescence light. These PMTs have a photon detection efficiency (PDE) of about 30%. That is the point where the First Auger Multi pixel photon counter camera for the Observation of Ultra-high-energy cosmic ray Showers (FAMOUS) may improve the detection of fluorescence light. The idea is to replace the PMTs with new semi-conductive light sensitive devices called *silicon photomultipliers* (SiPMs) which promise a higher PDE than PMTs. Since SiPMs have a rather small sensitive area of 1 mm^2 to 25 mm^2, the light has to be concentrated by special light funnels called Winston cones. Winston cones are non-imaging devices. The light leaves the Winston cone with a wide exit angle distribution from 0 to 85°, even if the light enters the Winston cone vertically.

[1] EeV = 10^{18} eV

The goal of this thesis is to evaluate the relative photon detection efficiency of SiPMs at different incident angles which is important for simulations of the overall performance of FAMOUS and later reconstructions.

This thesis starts with a short introduction to cosmic rays in general and gives an overview of the techniques used at the Pierre Auger Observatory to detect ultra-high-energy cosmic rays. Additionally the working principle of the fluorescence detection is described and a introduction to FAMOUS is given in chapter 2.

In chapter 3, the working principle of PIN-photodiodes, avalanche photodiodes and SiPMs is described.

Afterwards in chapter 4, a description of the experimental setup, the data acquisition and the data analysis is given. These studies require profound theoretical knowledge of the Fresnel equations and the behaviour of light when moving between media of differing refractive indices. Finally, the measurements depending the angular dependence of the relative photon detection efficiency of SiPMs are shown and discussed.

2. Cosmic Rays and Fluorescence Detection

V. Hess measured the ionization rate of air as a function of altitude at several balloon flights up to 5 km in 1912. At this time, the assumption was that the amount of ionizing radiation would decrease with distance from earth but Hess found an increase of radiation[1]. He concluded that the radiation must have its origin in cosmos. Later in 1925, his discovery was confirmed by R. Millikan who named the radiation *cosmic rays* [1].

Newer measurements reveal that the primary particles with energies up to 1 PeV[2] (knee) consist of 86% protons, 11% α-particles, 2% electrons and 1% heavy nuclei which hit our atmosphere producing secondary particles, Cherenkov light and fluorescence light due to excitation of atmospheric nitrogen molecules [3]. The cascade of secondary particles is called an *extensive air shower*. Above our atmosphere, cosmic rays include all stable particles with lifetimes of 10^6 years, also antiprotons and positrons are part of the primary particles [2].

These particles have a wide range of kinetic energy from a few MeV to at least 10^{20} eV and a related number of appearances in our atmosphere as shown in figure 2.1 and 2.2. To emphasize the features of the spectrum, the differential energy spectrum has been multiplied by the energy $E^{2.6}$. The flux decreases steeply from 1,000 particles per second and square meter at low energies, to one particle per century and square kilometre at energies above 100 EeV which is much higher than anything achieved by human build accelerators. The spectrum follows a power law and decreases with the energy E as described by formula

$$\frac{dN}{dE} \sim E^{\gamma} \tag{2.1}$$

where γ, called the spectral index, is a factor between -3.1 and -2.7. The spectral index has a value of -2.7 up to energies $E_k = 10^{15}$ eV - 10^{16} eV. At this region, called the *knee*, the spectral index γ changes from -2.7 to -3.1. One possible explanation is that the knee represents the upper limit of energies, protons can achieve from

[1] after a decrease of the radiation up to an altitude of 1 km

[2] PeV = 10^{15} eV

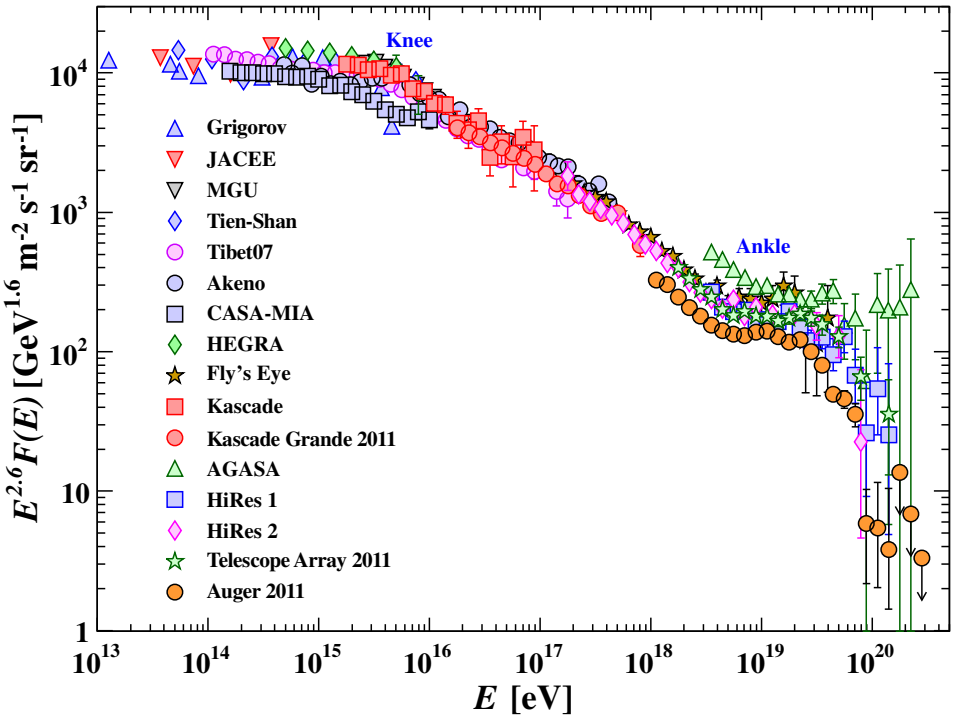

Figure 2.1: Energy spectrum of cosmic rays measured by various experiments. Shown is the flux as a function of the energy E. At the point called "knee" the spectral index γ changes from -2.7 to -3.1 and later at the point called "ankle" back to -2.7 [2]. Please note that the ordinate has been multiplied by E $^{2.6}$ to make the variation of the differential flux more visible.

galactic supernovae. The second feature between an energy of $E_a = 10^{18}$ eV - 10^{19} eV is called the *ankle* where the spectrum flattens again. The existence of the ankle could be an leakage of particles from our Galaxy since the magnetic fields are to weak to keep them. Sources of particles with such high energies are supposed to be of an extragalactic population [1].

The knowledge about the composition of cosmic rays and their origins is presently limited wherefore cosmic-rays are studied at several observatories all over the world. One of these observatories is the Pierre Auger Observatory in Argentina which has a detection area of 3000 km^2. This large area is necessary since high energy cosmic rays (UHECR) with an energy higher than 10^{19} eV have a extreme low flux of one particle per year and km^2. There are 1600 water Cherenkov detectors placed on this area with 1.5 km spacing. Each detector uses three photomultiplier tubes to detect the Cherenkov light emitted by the incoming particles when they propagate through the water [4].

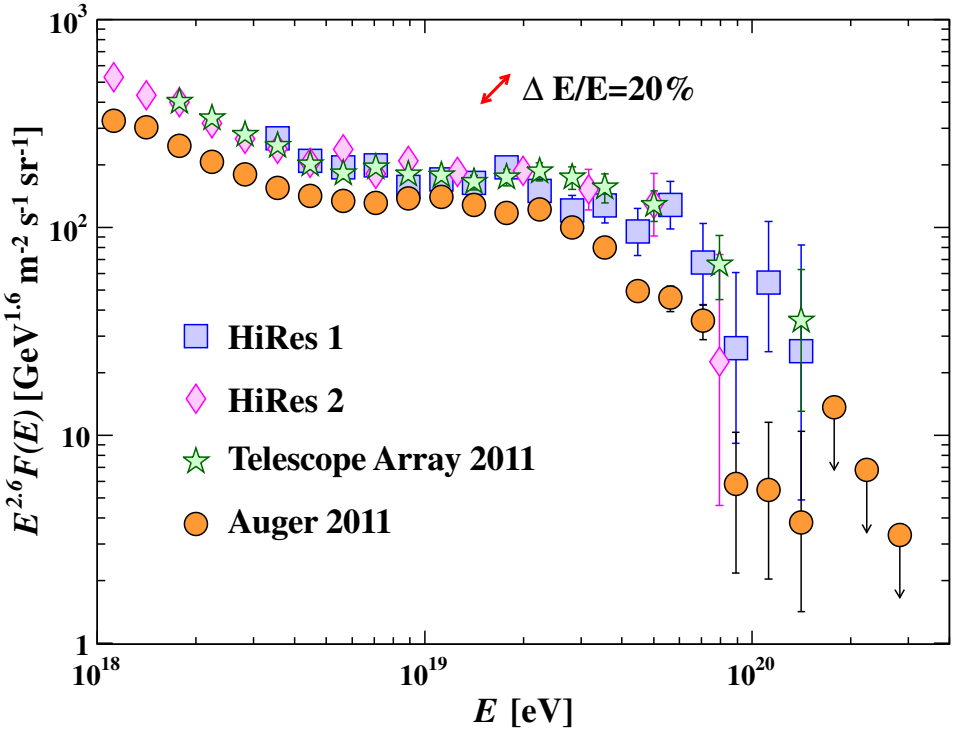

Figure 2.2: Zoom in of the plot 2.1: Shown are energies from 10^{18} eV to $10^{20.5}$ eV. Clearly visible is the point called *ankle* of the power spectrum where the spectral index γ changes back to -2.7 at $\approx 10^{18.5}$ eV [2].

Furthermore, there are 24[3] telescopes grouped in four buildings, which see over the surface detector to observe the longitudinal development of the shower by detecting the fluorescence light created by the incoming particles in the atmosphere [4]. Using the information from the fluorescence light, the arrival direction, the shower and particle energy and the point of maximum shower development $X_{\max}$ can be reconstructed [6]. Measurements of the fluorescence detectors are more accurate compared to measurements performed by the surface detector, but the main disadvantage is the small duty cycle since operation is only possible during moonless nights. Each telescope has a 12 m^2 spherical mirror with a curvature radius of 3.4 m and a camera consisting of 440 photomultiplier tubes.

Additionally, there are three extra fluorescence detectors which are called High Elevation Auger Telescopes (HEAT). This extension makes measurements of showers with higher altitudes possible. In combination with the infill and HEATLET array with a surface detector spacing of 750 m each, HEAT is supposed to measure showers with lower energies. A prototype radio-telescope array called Auger Engin-

[3]There are three additional telescopes of the HEAT extension

eering Radio Array (AERA) for detection of radio-emission from the showers and research and a development project on detecting microwave emission from shower electrons is also operated at the Pierre Auger Observatory [5].

The number of electrons and positrons created in the atmosphere during an extensive air shower, carrying about 90% of the energy, is given approximately by the Gaisser-Hillas function 2.2 [1]:

$$N_{e\pm}(X) = N_{max}\left(\frac{X - X_0}{X_{\max}}\right)^{\frac{X_{\max}-X}{\Lambda}} \cdot exp\left(\frac{X_{\max} - X}{\Lambda}\right) \tag{2.2}$$

The principle of fluorescence shower detection is shown in fig. 2.3. The fluorescence light comes through an entrance opening and is focused by the spherical mirror onto an array of photomultiplier tubes (PMTs) which detect the light. As mentioned before, these PMTs only have a photon detection efficiency (PDE) of about 30%.

This is the point where the First Auger Multi pixel photon counter camera for the Observation of Ultra-high-energy cosmic ray Showers (FAMOUS) telescope may improve the detection of fluorescence light. It is an SiPM-based fluorescence telescope prototype, because the improvements of the capabilities of PMTs are limited and there are new technologies like SiPMs which can nowadays reach absolute PDEs of about 35% [7, 8] and in future probably much more[4].

For FAMOUS, the light will be focussed by a Fresnel lens on a system of 64 Winston cones which concentrate the light onto the SiPMs located underneath (fig. 2.4). A Winston cone is a parabolic light concentrator with a overall transmission efficiency of 90%[5] as simulations show. Since Winston cones are non imaging devices, the light leaves the Winston cones at different angles from 0° to 85° and hits the SiPM. For this reason, the angular dependence of the relative photon detection efficiency is studied in this thesis. Each pixel of FAMOUS has a field of view (FOV) of 1.5° x 1.5° resulting in a total field of view of 12° x 12° FOV. A prototype of FAMOUS with 7 pixels is being build at the moment and is meant to measure first light this year [11].

Main part of FAMOUS are the SiPMs arranged underneath the Winston cones, thus the next chapter deals with the theory of SiPMs.

[4]Prototypes are promising absolute photon detection efficiencies up to 60% in the near UV-blue wavelength range (350 nm - 500 nm) with a significantly reduced crosstalk and afterpulse probability (more information in chapter 3)[9]

[5]Assumed was a perfectly smooth surface

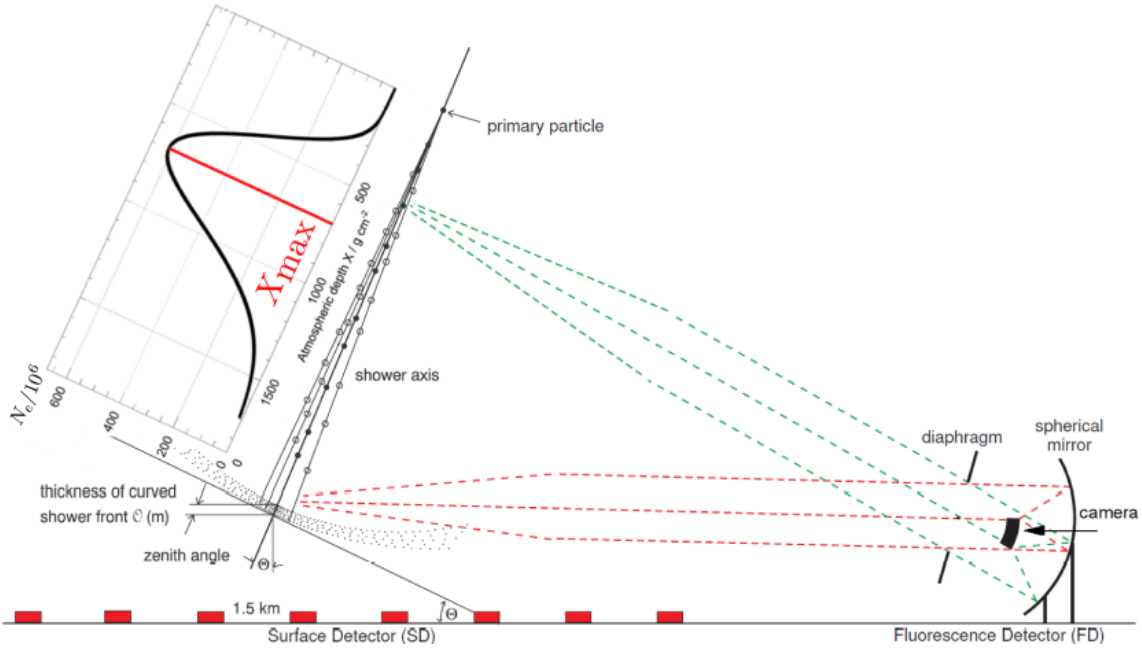

Figure 2.3: Working principle of the Pierre Auger Observatory. Note the surface detectors with a spacing of 1.5 km and on the left the fluorescence detector. The field of view of the fluorescence detector encloses the shower axis to reconstruct properties of the shower (energy, X_{max}, direction). Next to the shower axis, a typical plot of the Gaisser-Hillas function is shown. Taken from [11]

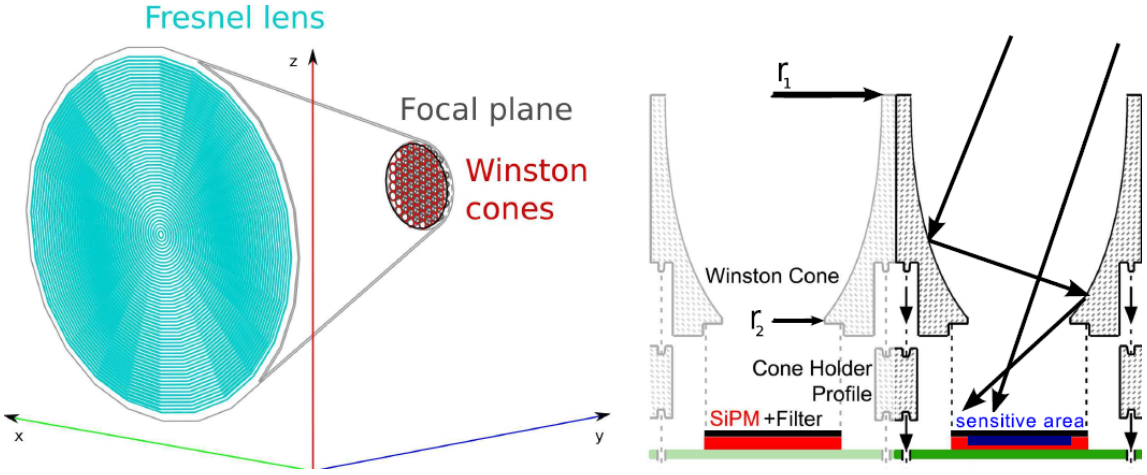

Figure 2.4: Left: Simulation of FAMOUS with a Fresnel lens (f = D = 510 mm) made of UV transparent PMMA (Polymethylmethacrylat, commonly referred to acrylic glass) to focus the light on the Winston cones (r_1 = 6.7 mm, r_2 = 3 mm). **Right:** Shown is a cross section of the focal plane of FAMOUS. The fluorescence light is concentrated on the SiPMs by the Winston cones. Taken from [10, 11]

3. Silicon Photomultipliers

3.1 Introduction

Silicon photomultipliers (SiPMs) are a new kind of photon detection device that is still in its infancy. At the current state of development, this technology promises absolute photon detection efficiencies up to 60% in the near UV blue wavelength range (350 nm - 500 nm) [9]. This is a great improvement compared to the PDE of 30% achieved using the photomultiplier tubes (PMTs) at the Pierre Auger Observatory in Argentina. PMTs typically utilize a operation voltage of about 1000 V to accelerate electrons towards the dynodes, SiPMs only need about 100 V [13].

An SiPM is an array of Geiger-mode avalanche photo-diodes. "Geiger-mode" describes the feature that if an electron-hole pair is created by an incoming photon, the high electric field inside the diode causes an avalanche process where more and more charge carriers are generated due to impact ionisation. Thus, SiPMs reach high signal gains which allows to measure single photons [13]. The following sections describe the design and development from the first PIN-photodiodes to SiPMs.

3.2 PIN-Photodiode

The PIN-photodiode consists of a thick, high-ohmic semiconductor between two doped n+ and p+ regions (fig. 3.1). When light enters the photo-diode, an electron-hole pair can be created due to the photoelectric effect. For silicon, the energy required to generate an electron-hole pair is 3.6 eV, a higher energy of the photon

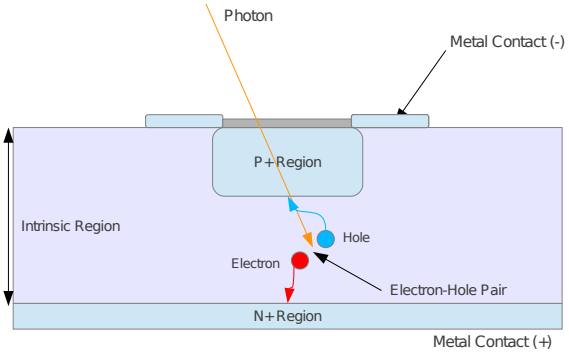

Figure 3.1: Structure of a PIN-photodiode. The intrinsic region of the semiconductor is embedded between the p+ and the n+ region.

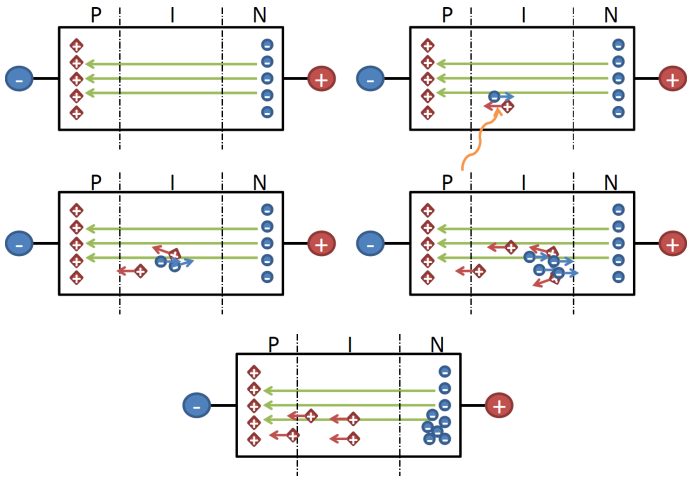

Figure 3.2: Shown is an avalanche process inside an APD. The order is to be read from left to right and top to bottom. The electric field due to the applied operation voltage V_{OP}, is symbolized by the green arrows. A photon hits the APD and creates an electron-hole pair which gains enough energy to create another one by impact ionisation. This continues to an avalanche process. Taken from [12].

leads to a higher kinetic energy of the electron in direction of the conduction band. Inside the n+ doped region, the pure silicon is doped with atoms which can provide extra electrons to the conduction band. Similar to the n+ doped region, the p+ doped region is doped with acceptors which are able to catch weakly bound electrons. Due to the interaction between the two regions, there is a small electric field which moves the electrons towards the p-layer and the "holes" to the n-layer. The separated charges can be detected as a current providing that they do not recombine inside the semiconductor first [13].

The layer of intrinsic silicon reduces the capacitance of the diode and through this, the serial noise. In addition, the sensitivity for longer wavelengths (red and infra-red light) increases due to the longer absorption length. The top p-layer has to be highly doped, but also needs to be transparent for incoming light. Usually, the surface of the PIN-photodiode is covered by a layer of highly transparent resin to protect the bond wires and prevents the very thin p+ layer from mechanical damage.

Since the electric field inside the diode is very weak, there have to be hundreds of photons to create a signal above the noise. This noise increases proportionally to the area because of the increasing capacitance of the diode. The next section deals with avalanche photodiodes which have an higher gain due to an applied electric field and thus, can detect a lower photon flux [13].

3.3 Avalanche Photodiodes

The main difference of avalanche photodiodes (APD) to PIN-photodiodes is a high electric field at the junction of the positive and negative doped silicon. As a result of the electric field, the electron created at the impact of a photon is accelerated

and gains enough energy to create another electron-hole pair by impact ionisation. Furthermore, those two charge carriers can reach enough energy to generate other electron-hole pairs again and start an avalanche process. This process is illustrated in figure 3.2. The positively charged "holes" do not gain enough energy to ionize secondary atoms, since they have much more mass.

In principle, a gain of 10^4 is possible, but after a few hundreds, one has to make a great effort to regulate temperature and operating voltage because the APD is operated close to its breakdown voltage. Practical is a gain of 50-200.

The next section discusses "Geiger-mode" avalanche photodiodes where also the positive charge carriers are involved in the avalanche process which leads to a much higher gain.

3.4 Geiger-Mode Avalanche Photodiodes

3.4.1 G-APDs

Geiger-mode avalanche photodiodes (G-APDs) use a higher electric field than avalanche photodiodes (APDs) to cause self-sustaining avalanche processes triggered by electrons and holes. Due to the higher electric field, G-APDs have a much larger gain of about 10^5 - 10^7. To stop the avalanche process, the voltage has to be reduced, which may be realized with a high ohmic resistor (quenching resistor). The current produced in an avalanche process causes a voltage drop over the resistor and this reduces the voltage applied at the diode. The operating voltage falls below the breakdown voltage and the avalanche process stops. During recharge, the G-APD is not capable detecting other photons. Only if the whole process is completed, the G-APD can detect photons with full efficiency again. The time needed is called recovery time t_{rec}. The electric signal given by the G-APD is not related to the number of initially created electron-hole pairs and thus, any proportionality to the photon flux is lost [13].

3.4.2 Silicon Photomultiplier

To detect more than one photon at the same time, several G-APDs can be in parallel. A measurement of the photon flux is now possible due to the fact that several cells can break down at the same time, each of them giving a signal of around 50 mV if using a 50Ω load. The signal of an SiPM is shown in figure 4.9 on page 20. The dynamic range of an SiPM is given by the number of cells, but a linear response is only given for a number of photons, which is much smaller than the number of cells.

Beside the advantages of SiPMs stated in the beginning of this chapter, there are some disadvantages being discussed now.

3.4.2.1 Dark Counts

Avalanche processes cannot only be initiated by incoming photons. Dark counts are produced by thermal excitation and correlated noise caused by optical crosstalk and afterpulsing. The two kinds of correlated noise are:

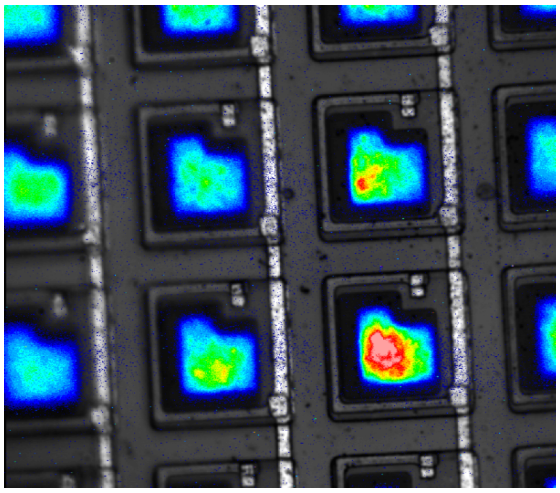

Figure 3.3: Shown is a picture of an SiPM operated above the breakdown voltage. The light, emitted by the cells of the SiPM, is measured by integrating in darkness over several seconds. Adapted from [14].

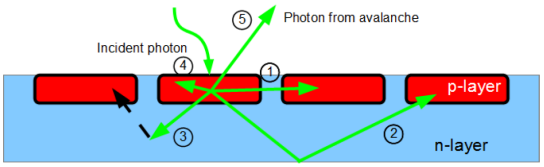

Figure 3.4: Scheme of the possibilities of optical crosstalk. **1./2.** Optical crosstalk caused by direct/indirect absorption in a neighboured cell. **3.** Photon is absorbed in the region of low electric field. Optical crosstalk can occur if the created electron-hole pair travels to the region of a high electric field. **4.** Photon is absorbed during an avalanche breakdown, therefore no optical crosstalk. **5.** Photon leaves the SiPM. Taken from [7].

Optical Crosstalk During an avalanche process, roughly 10^5 free charge carriers are created and also about 3-30 photons due to recombination (fig. 3.3) [7]. Of these photons, those with an energy higher than the band-gap of silicon, can travel to another cell of the SiPM and cause a breakdown there. A sketch of this process is shown in figure 3.4.

Afterpulsing Afterpulsing occurs when charge carriers from the original avalanche process are trapped on an impurity of the silicon. After 10 ns - 100 ns, the release of the charge carriers may cause another breakdown of the cell [13]. Measurements of these effects can be found in [7].

It is obvious, that dark counts produced by thermal excitation become more if the temperature rises, but also the breakdown voltage depends on the temperature. The overvoltage $V_{\mathrm{OV}} = V_{\mathrm{Bias}} - V_{\mathrm{BD}}$ affects the gain strongly, so it is important to know the exact breakdown voltage V_{BD}. The gain $G = \Delta Q/e$ is linear dependent on the overvoltage as described by formula 3.1 where ΔQ is the charge generated by one cell firing:

$$\Delta Q/cell = C \cdot (V_{Bias} - V_{BD}) \tag{3.1}$$

This characteristic is used to determine the breakdown voltage before the measurement of the relative photon detection efficiency starts. More information in chapter 4.2.

4. Relative Photon Detection Efficiency

As described in chapter 2, FAMOUS will consists of an array of 64 Winston cones with an array of SiPMs arranged underneath (fig. 2.4 on page 7). Based on the geometry of the Winston cones, light which does not simply go through the Winston cone, can be reflected several times and may leave the Winston cone at various angles. In figure 4.1 and 4.2 is a simulation taken from [15] shown. As one can see, the light leaves a not perfect polished Winston cone at nearly all angles up to 85°. This results in a transmission coefficient of 79% for a lobed surface[1].

To consider the use of Winston cones as light concentrators, one has to know about the photon detection efficiency (PDE) of silicon photomultipliers (SiPMs) at different incident angles. This is discussed in this chapter and is the central point of this thesis.

4.1 Experimental Setup

A sketch and a picture of the measurement setup for the measurement of the relative photon detection efficiency is shown in figure 4.3. The main part of the setup is located in a dark box to avoid external light. The SiPM is placed on the front of an aluminium box manufactured by the mechanics workshop (fig. 4.4). The SiPM is connected to the amplifier board located inside the aluminium box. The amplifier board is powered by the NIM module *APDPI 2.0* which provides, additionally to the operating voltage of the amplifier board, the bias voltage for the SiPM (fig. 4.6). To control the amplifier board, there is also a USB connection for the laptop.

The box itself is mounted on a stepper motor (RB-Soy-22) which can perform steps of 1.8° with a step angle accuracy of 5% [16]. The whole system is mounted on an optical bench to get a high accuracy in the adjustment of the SiPM relative to the light spot. It has been verified that the SiPM is located in the middle of the light spot using a very bright LED torch. The stepper motor is powered and controlled by a programmable Arduino Uno[2] which is connected to an Arduino motor shield[3].

[1] 50% spike reflection means, that 50% of the light gets reflected by $\Theta_{incoming} = \Theta_{reflected}$ but the remaining 50% are reflected in random direction due to the lobed surface

[2] http://arduino.cc/en/Main/ArduinoBoardUno

[3] http://arduino.cc/en/Main/ArduinoMotorShieldR3

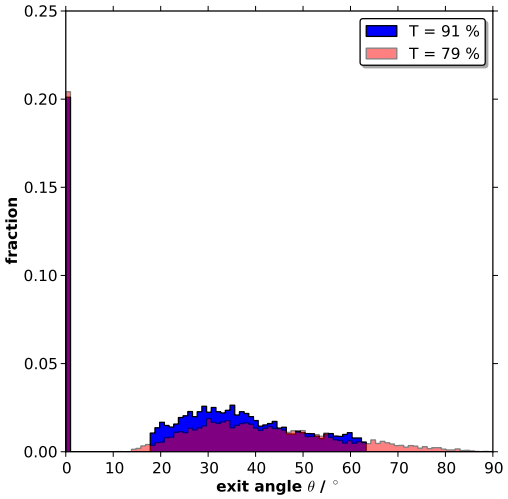

Figure 4.1: Simulation: Shown is the fraction of photons in dependence on the exit angle. The blue data represent a Winston cone with a perfect smooth surface. The pink coloured data represents a lobed, ragged surface of the Winston cone with 50% spike reflection [15]. Exit angles up to 85° have been found with a transmission of 79%.

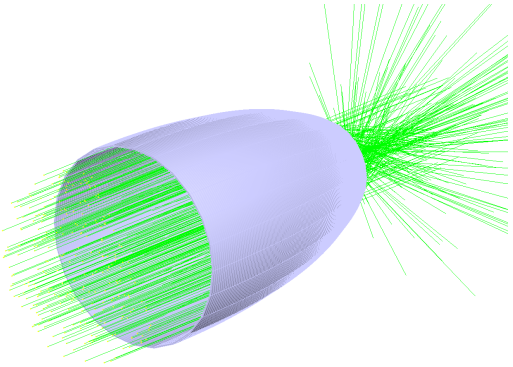

Figure 4.2: 3D Simulation of a Winston cone, created with the GEANT4 Framework. The light leaves the Winston cone at many different angles [10].

For this purpose, a program for the Arduino has been written to control the stepper motor using a laptop. Additionally, a response system has been written to verify that requested actions were performed successfully. After every request, the Arduino is programmed to repeat the request and also to give information about what action it will perform. Requests of a false length are ignored by the Arduino to avoid wrong actions due to damaged packets. A typical request would be ”001;F;D”. The Arduino interprets this as: ”Send the stepper motor the signal to perform one step forward in double-coil mode[4]”. Also a measurement of the angular accuracy of the stepper motor has been undertaken. For the analysis see chapter 4.4.2.

An Arduino is an open-source single-board micro-controller which can be programmed using a Wiring-based language (syntax and libraries), similar to C++. Wiring is an open-source programming framework for micro-controllers. ”The idea of Wiring is to write a few lines of code, connect a few electronic components to the hardware and observe how a light turns on when person approaches to it, write a few more lines add another sensor and see how this light changes when the illumination level in a room decreases”[5]. So, there are libraries to communicate with the extras available,

[4]The coils of the stepper motor are energized in pairs, so it produces 100% the nominal torque of the motor

[5]http://wiring.org.co

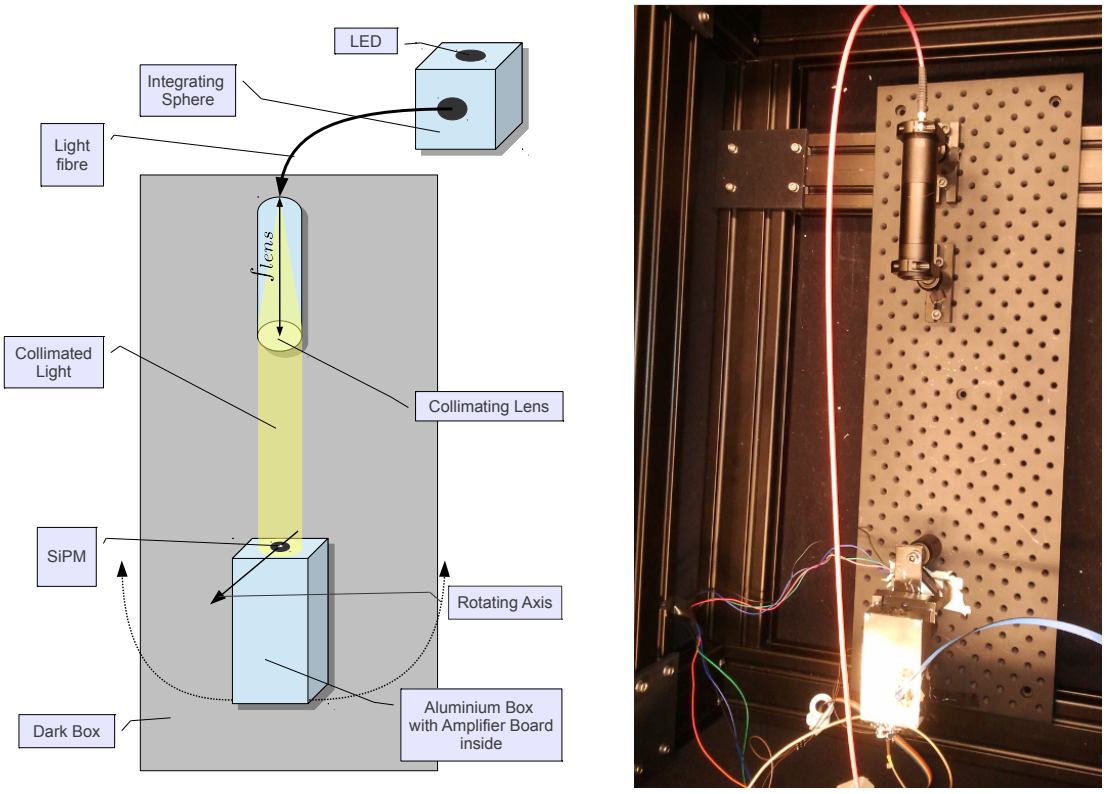

Figure 4.3: Left: Sketch of the measurement setup. The light of an LED, which is attached inside an integrating sphere, is put into the dark box via a light fibre. Inside the dark box, the fibre is mounted on a lens tube. The fibre is exactly located in the focal length of the plano-convex lens, thus collimated light illuminates the SiPM. **Right:** Picture taken from the setup. Later, the aluminium box has been painted with a matt black varnish to avoid reflections.

e.g. sensors or the stepper motor used for this bachelor thesis which is connected to the Arduino.

To illuminate the SiPM uniformly, the light of a flashed light-emitting diode (LED) is put into an integrating sphere. An integrating sphere is a hollow, spherical optical component which is covered inside with a white diffusing coating to eliminate all inhomogeneities of the original light distribution. Thus, a uniform distribution of light is emitted to all exit ports. From one port of the integrating sphere, a light fibre with a diameter of 200 µm leads the light into the darkbox where the fibre is attached to the back of a lens tube. A plano-convex lens with a focal length of 12 cm is located in the front of the lens-tube, so that the light fibre is located in the focal point of the lens. Because of the screw thread inside the lens-tube it is possible to position the lens very precisely. Hence, it is possible to collimate the light very well. Due to the small diameter of the light fibre (200 µm) the collimation becomes better because it can be approximated as a point source. A measurement has been performed to assure the homogeneity and collimation of the light. This can be found in section 4.4.

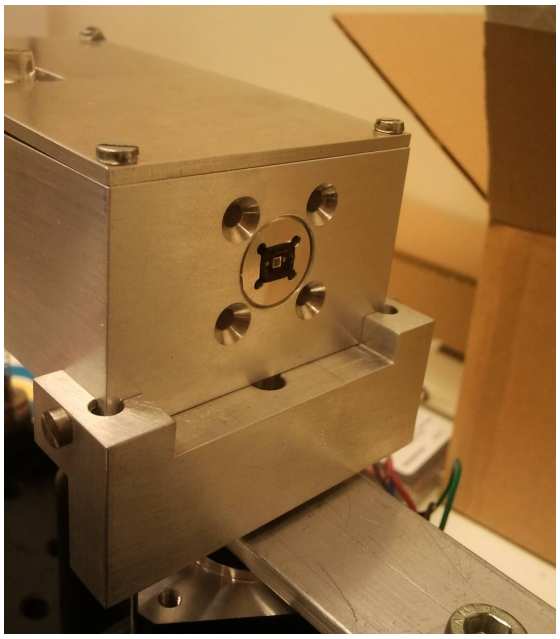

Figure 4.4: Picture of the SiPM mounted on top of the rotating axis of the aluminium box. Later, the aluminium box have been painted with a matt, black varnish.

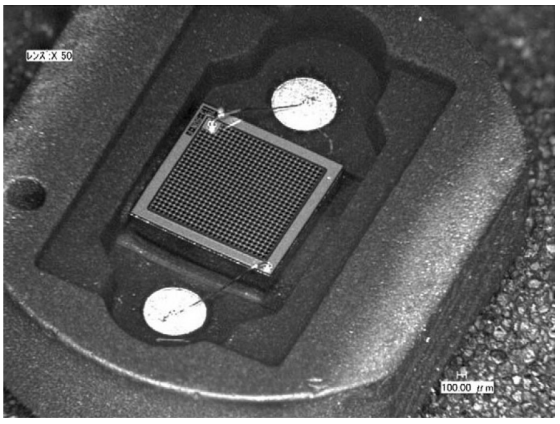

Figure 4.5: Picture of an SiPM taken with a microscope [12].

4.2 Procedure and Data Acqisition

The overall concept was to create a fast fully automatic measurement of the relative photon detection efficiency for a certain LED without intervention to minimize external disturbances.

A C++ program has been written which permits a fully automated measurement of the angular dependency of the relative photon detection efficiency for a given LED. During the measurement, the laptop is connected via USB to the WIENER VM-USB, the Arduino and the APDPI 2.0. A sketch of the data acquisition is shown in figure 4.6.

The VM-USB is an USB-interface for signal transmission between the hardware inside the VME/NIM hybrid-crate, e.g. the QDC (charge-to-digital converter) and a personal computer. Additionally, the VM-USB has two outputs (O-1 and O-2) for outgoing NIM-pulses. These signals can be modified in frequency or width of the pulses. The output O-1 of the VM-USB module provides the gate for the QDC and O-2 provides the signal for the coincidence (fig. 4.9). While the gate (O-1) is open, the QDC integrates the deposited charge on all channels. A typical QDC spectrum is shown in figure 4.7. The second output is directly connected to the coincidence. The output of the coincidence is used to trigger a pulse generator which in turn generates pulses of ≈ 8 ns length to flash the LED.

Changing the frequency of the signal via O-2 to 0 Hz, the LED is turned off or on the other hand, changing the frequency to a very high value[6], the LED is flashed at the frequency given by signal O-1. This is important for the measurement of the dark counts due to thermal excitation before each run, when the LED has to be turned off. See chapter 4.3 for more details about the analysis method.

During the measurements with the LED being flashed, a short LED pulse of approximately 8 ns is used to get only the photon induced breakdown of a cell and no afterpulses. A frequency of 50 kHz is used to reduce the time needed for acquiring the 100,000 QDC counts for each histogram. At 50 kHz, the pulse interval is still large enough for the analysis not to be disturbed by afterpulses from previous flashes.

As mentioned in section 3.4.2 the overvoltage $V_{\mathrm{OV}} = V_{\mathrm{Bias}} - V_{\mathrm{BD}}$ is temperature dependent and determines the gain, the thermal noise rate and the absolute PDE. Thus one has to wait till the temperature is constant inside the dark-box. Since the flux of light is very low, a determination of the breakdown voltage is performed as described in [7] before each measurement of the relative photon detection efficiency to optimize the gain. The breakdown voltage is expected to be linearly dependent on the temperature as described by formula 3.1 on page 12.

The mean distance $\Delta Q = Q_{i+1} - Q_i$ between two peaks in the QDC spectrum (fig. 4.7) corresponds to the deposited charge per fired cell. The position of the first and second peak were determined by using the class *TSpectrum* of the analysis framework ROOT. The libraries of the ROOT framework can be used to handle and analyse large amounts of data very efficiently[7]. Afterwards function 3.1 is fitted to the data returning the breakdown voltage as y-axis intercept.

Using the APDPI 2.0, the bias voltage V_{Bias} for the SiPM is set to 1.3 V above the previously determined breakdown voltage to optimize the gain and thus, the absolute PDE. The QDC is connected to the *fast out* LEMO connector of the amplifier board to get the signals of the SiPM (fig. 4.9).

Afterwards, the main measurement starts. For every incident angle at an interval of 1.8°, a QDC spectrum with $100,000$ entries is taken, saved on the HDD of the laptop and analysed later. For each LED, the angle of incidence is varied up too 100.8° in one direction. Afterwards, the stepper motor moves back to 0° and the same procedure is done again up to $-100.8°$. This leads to 56 QDC spectra for each direction. A QDC spectrum is the deposited charge spectrum from an SiPM taken with the QDC. To estimate the dark rate caused by thermal excitation, a measurement with a turned off LED is taken at the start of each run for a certain LED. Two QDC spectra at different incident angles are shown in figure 4.7 and 4.8. The first peak is the *pedestal* where no photon has been detected by the SiPM. The second peak is called the *one photon equivalent peak* (1 p.e.) where one photon has been detected and so on. In comparison to the QDC spectrum taken at 50.4° degree, one can see that the pedestal at 0° is smaller, so more photons have been detected. The next chapter deals with the analysis of these spectra.

[6]"Very high" means as it were a constant signal

[7]http://root.cern.ch/

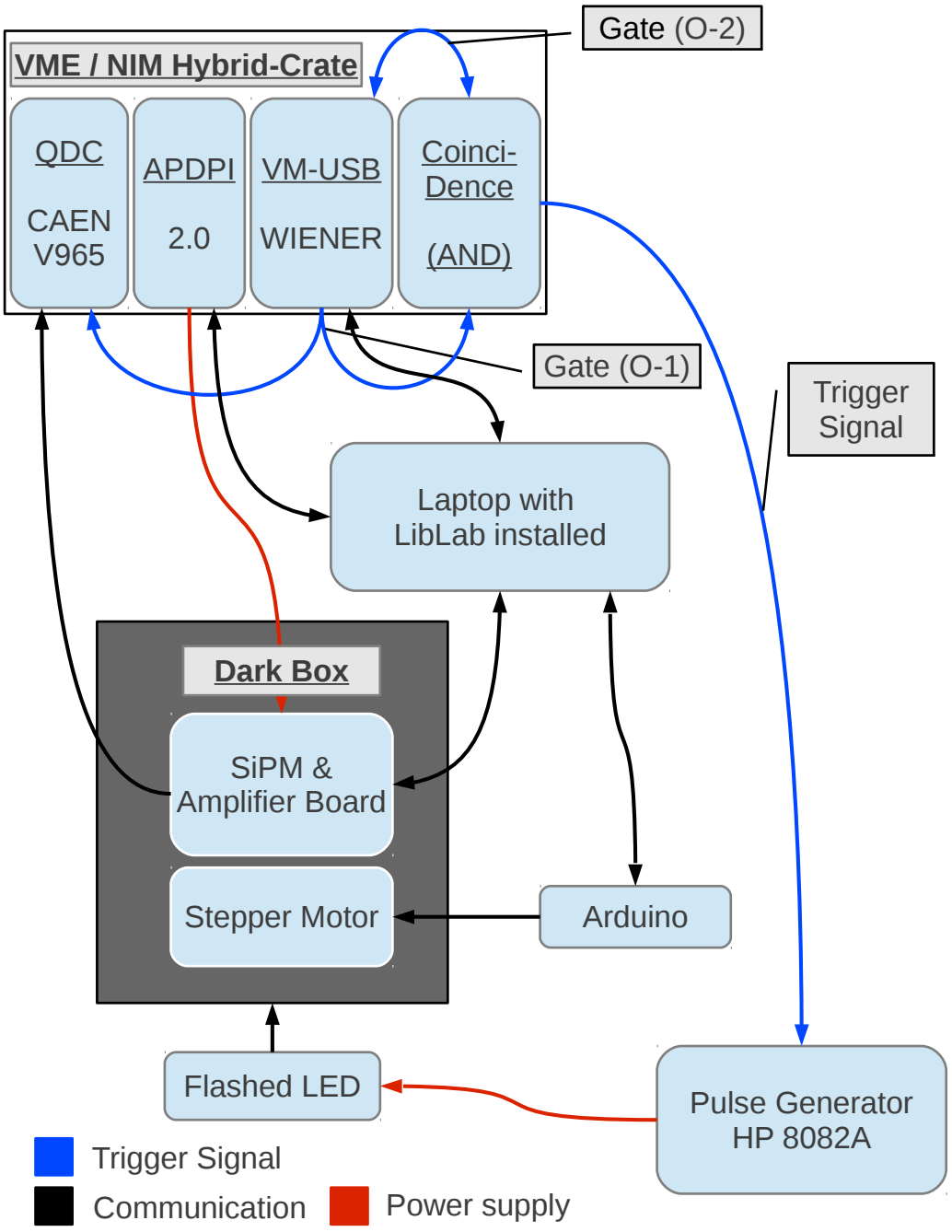

Figure 4.6: Sketch of the data acquisition of the PDE measurement: The laptop is connected via USB to the VM-USB which provides the communication to the internal VMEbus of the VME/NIM-crate. The signal outputs O-1 and O-2 of the VM-USB are connected with the coincidence which gives the signal to the pulser for pulsing the LED. Output signal of O-1 provides also the gate (fig. 4.9) for the QDC. The Arduino controls the stepper motor, getting the commands from the laptop. The APDPI supplies the amplifier board inside the dark box and thereby also the SiPM.

4.3 Data Analysis Method

The goal of this analysis method is to obtain the relative photon detection efficiency at different incident angles without the distorting effects of thermal noise and crosstalk and afterpulses, also called *correlated noise*. A picture of an amplified SiPM signal is shown in figure 4.9 and an associated QDC spectrum is shown in 4.7. The first peak of the spectrum corresponds to the baseline of the oscilloscope where no photon has been detected and is further called *pedestal peak*. The following peaks are the *one photon equivalent peak*, the *two photon equivalent peak* and so on. These peaks corresponds to the pedestal line, the one p.e. signal and two p.e. signal in the oscilloscope picture 4.9.

Crosstalk and afterpulses can only occur if at least one cell has fired. Consequently, the pedestal peak is not affected by correlated noise. This is used by the analysis method. Under the assumption, that the distribution of fired cells follows a Poissonian distribution[8], the mean number of fired cells μ can be calculated from the probability P(μ,0) that no photon has been detected. This is equal to the number of normalised entries N_{ped}/N_{tot} in the pedestal peak [8]:

[8]If we assume that there is a probability for no cell-breakdown or a cell-breakdown, we can calculate the probability for two, three or more cell-breakdowns from the Binomial distribution. For a high number of "trials" the Binomial distribution converges towards the Poisson distribution.

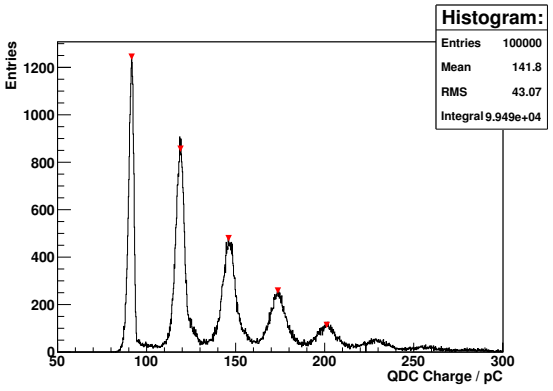

Figure 4.7: Charge spectrum taken from the QDC at an incident angle of 0°. First peak is the pedestal where no photon has been detected by the SiPM. The second peak is equivalent to one photon and so on.

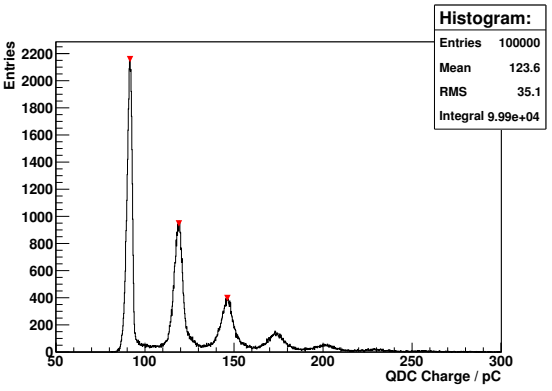

Figure 4.8: Charge spectrum at an incident angle of 50.4°. The pedestal is much bigger than before at 0°, thus less photons have been detected. Please note that the y-axis scale has changed.

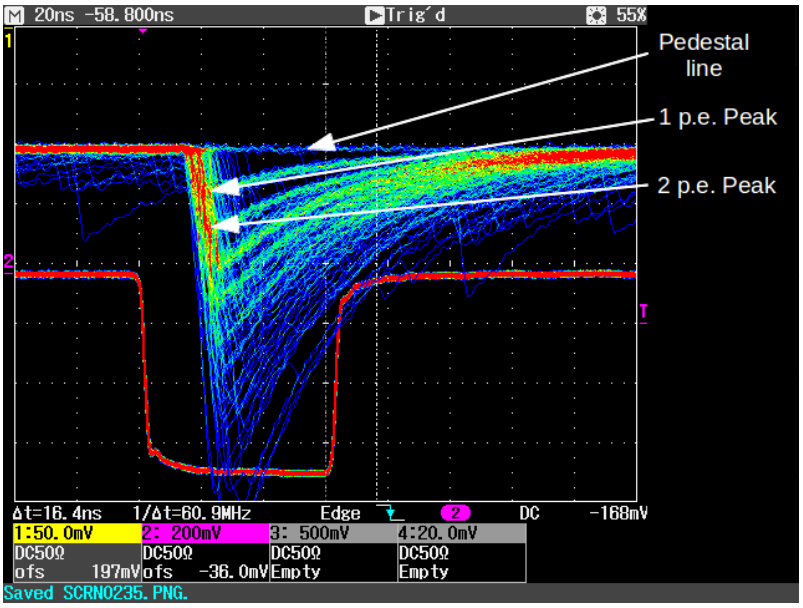

Figure 4.9: Picture taken with the oscilloscope of an 1x1 mm^2 SiPM (channel 1) amplified with a flashed LED. Channel 2 was used to trigger the LED and is also the gate of the QDC. Clearly visible, the baseline corresponding to the pedestal in the QDC spectra (fig. 4.7), where no photons have been detected. Also visible are the one and two photon equivalent (p.e.) peaks which also can be seen in the QDC spectra. Shown on the x-axis is the time (1 division $\widehat{=}$ 20 ns, on the y-axis the voltage (1 division $\widehat{=}$ 50 or 200 mV (channel 1 & channel 2)).

$$P(\mu, k) = \frac{\mu^k \cdot e^{-\mu}}{k!} \tag{4.1}$$

$$\Rightarrow P(\mu, 0) = e^{-\mu} \tag{4.2}$$

$$\Leftrightarrow \mu = -\ln\left[P(\mu, 0)\right] \tag{4.3}$$

$$\Leftrightarrow \mu = -\ln\left(\frac{N_{\text{ped}}}{N_{\text{tot}}}\right) \tag{4.4}$$

In this derivation, k is the number of occurrences of cell breakdowns (events) and μ is the mean of detected photons by the SiPM. To calculate the mean number of detected photons, we use $P(\mu, 0)$ because this value is given by the fraction of entries in the pedestal peak N_{ped} and the total number of measured events N_{tot} since it is not affected by correlated noise.

The number of entries in the pedestal peak is determined by integrating the spectrum from the beginning up to the 0.5 p.e. level. N_{tot} is given by the integral over the total spectrum. In this bachelor thesis, 100,000 events have been taken for every QDC histogram, thus N_{tot} is always equal to $100,000$. The statistical uncertainty of the number of events in the pedestal is given by the binomial error:

$$\sigma_{N_{\text{ped}}} = \sqrt{N_{\text{tot}} \cdot p(1-p)} \tag{4.5}$$

$$\Rightarrow \sigma_{N_{\text{ped}}} = \sqrt{N_{\text{ped}} \left(1 - \frac{N_{\text{ped}}}{N_{\text{tot}}}\right)} \tag{4.6}$$

Now μ represents the average number of fired cells without the effects of correlated noise. Nevertheless, thermal noise affects the pedestal peak. To correct for thermal noise, we calculate the mean number of detected photons μ_{dark} while the LED was turned off and subtract it from μ_{light} obtained by measurements with a flashed LED. Of course, the general conditions (e.g. temperature) must not change during the measurement of all other incident angles and are monitored over the total measurement duration.

Finally, the mean number of detected photons is given by:

$$\mu = \mu_{\text{light}} - \mu_{\text{dark}} \tag{4.7}$$

$$\Rightarrow \mu = \ln\left(\frac{N_{\text{tot}}}{N_{\text{ped}}}\right) - \ln\left(\frac{N_{\text{tot}}^{\text{dark}}}{N_{\text{ped}}^{\text{dark}}}\right) \tag{4.8}$$

Using Gaussian error propagation the error of μ is given by:

$$\sigma_\mu = \sqrt{\left(\frac{\sigma_{N_{\text{ped}}}}{N_{\text{ped}}}\right)^2 + \left(\frac{\sigma_{N_{\text{ped}}^{\text{dark}}}}{N_{\text{ped}}^{\text{dark}}}\right)^2} \tag{4.9}$$

The relative photon detection efficiency at a certain incident angle is derived from the Poissonian mean μ using formula 4.10. The cosine factor corrects the loss of area while turning the SiPM. The uncertainties depending the relative PDE are estimated numerically with a Monte Carlo simulation using Gaussian distributed random numbers since the error propagation leads to an $\tan(\Theta)^2$ which leads to overestimated errors for large angles due to the singularity of the $1/\cos(\Theta)$ at 90°.

$$\text{PDE}(\Theta) = \frac{\mu(\Theta)}{\mu(0°)} \cdot \frac{1}{\cos(\Theta)} \tag{4.10}$$

4.4 Validation of the Experimental Setup

One of the main characteristic of a well adjusted setup for measuring the relative photon detection efficiency is the symmetry of the taken data for negative and positive angles. An example of a not axially symmetric measurement is shown in figure

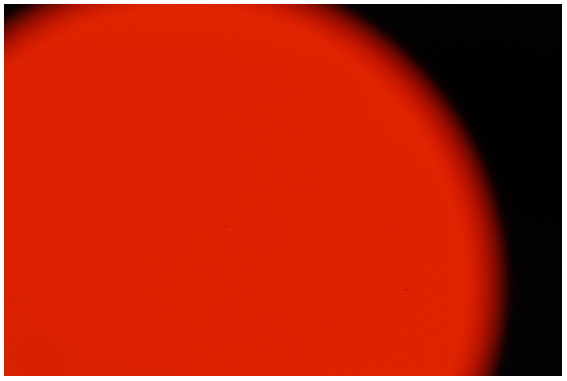

Figure 4.10: Raw picture of the collimated light spot taken with a camera without a lens, only using the CCD.

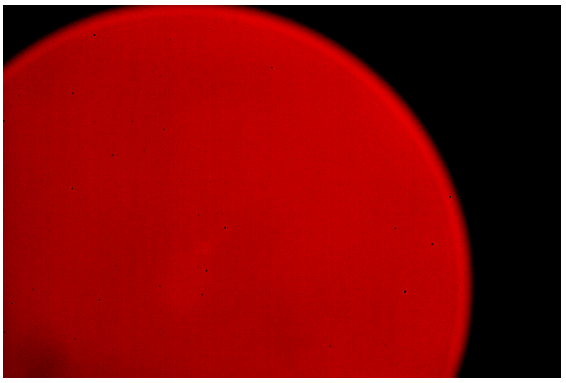

Figure 4.11: Same picture as shown on the left, but with applied adjustments to the colour levels of the picture. A slight inhomogeneity becomes visible, but a radial symmetry.

4.20 on page 31. If a measurement is performed in one direction only[9], one would measure a lower photon detection efficiency as expected by the Fresnel equations.

To ensure that the data taken with the setup is trustworthy, three tests have been performed. First, the homogeneity and the collimation of the light has been tested. Secondly, the angular accuracy of the stepper motor has been tested, of which the manufacturer states it to be about 0.9° [16], and at last, it has been checked if there is scattered light inside the box, especially at large angles.

4.4.1 Collimation and Homogeneity of the Light

Homogeneity: Testing the light for homogeneity is quite important if it is assumed that the SiPM is not positioned exactly on the rotating axis of the stepper motor. In that case, the SiPM would not stay at its horizontal position while turning it and thus, an inhomogeneity would distort the measurements.

Two measurements have been performed. On the one hand, a measurement was taken while the SiPM was located in the upper half of the light spot and on the other hand, a picture was taken from the light spot and analysed with a graphics editing program. To take the photo, a camera without a lens was used, so that the light hits the CCD[10] of the camera directly (fig. 4.10). Using the graphics editing program, the colour levels were shifted towards red to increase the contrast of the picture and possible inhomogeneities become visible (fig. 4.11). One can see a slight inhomogeneity but with a radial symmetry. The small black points are dust particles on the CCD and were not seen while inspecting the light spot with a piece of paper and a very bright LED torch. To be sure that the slight inhomogeneity does not change the outcome of the measurement, a measurement was taken while the SiPM

[9] e.g. only positive angles

[10] Charge-coupled device, an electronic light sensor used in digital cameras

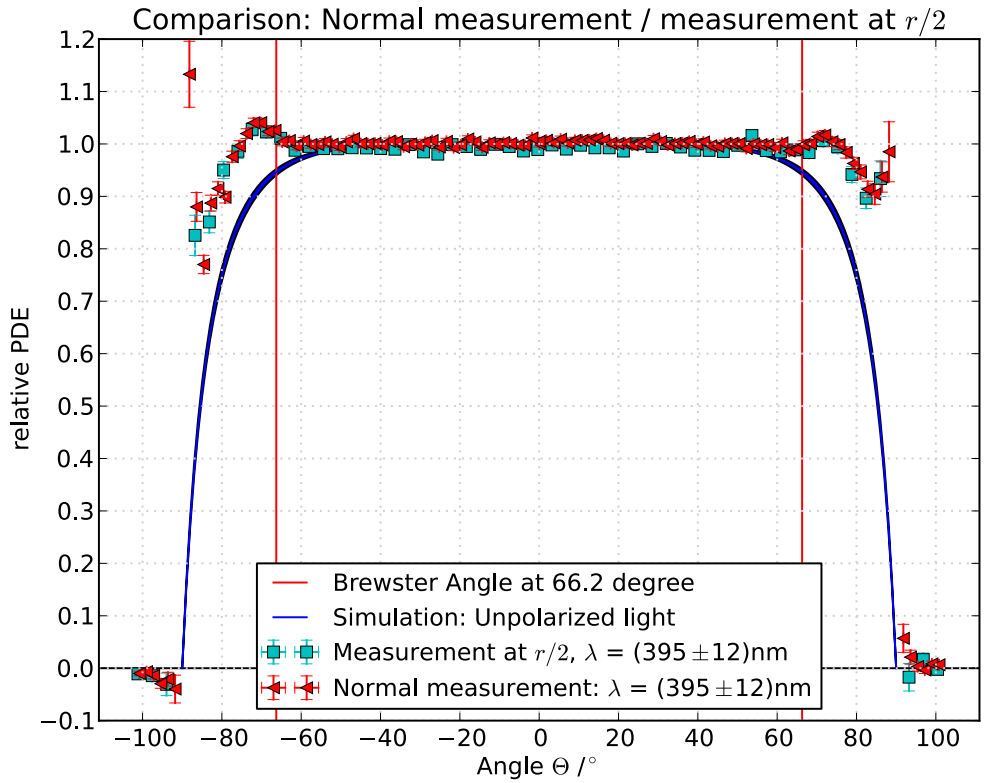

Figure 4.12: Comparison between a measurement done at the upper half of the collimated light spot and a measurement right in the middle of the light spot as during all later measurements. The shape of the measurement and why this measurement does no fit to the theory is discussed in section 4.6. Nevertheless, both measurements fit well, so the slight inhomogeneity does not change the outcome of the measurement.

was located in the upper half of the light spot. Afterwards, a measurement with the SiPM located in the middle of the light spot was taken and compared (fig 4.12). As one can see, there is only a change within the statistical fluctuations and it can assumed that the light is sufficient homogeneous.

Collimation: To test for collimation, the light of the bright LED torch was put into the light fibre. This light fibre was positioned in the focal lengths of the lens and the light was directed onto a wall on the opposite wall of the room. The spread of the light was calculated using formula:

$$\theta = \arctan\left(\frac{d_2 - d_1}{2 \cdot L}\right) = (0.26 \pm 0.10) \tag{4.11}$$

where $d_1 = (2.2 \pm 0.1)$ cm is the diameter of the source and $d_2 = (5.7 \pm 0.1)$ cm the diameter of the light spot after the distance $L = (3.96 \pm 0.05)$ m. One may note

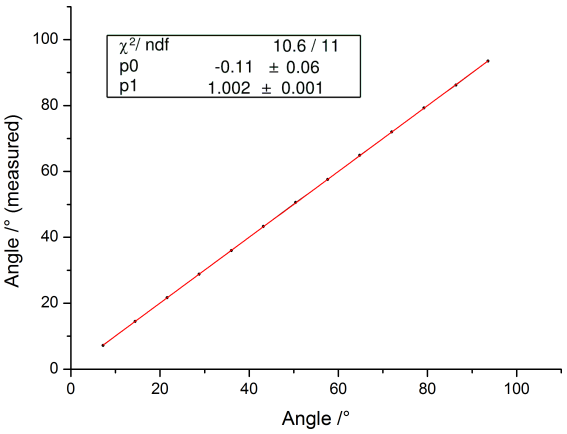

Figure 4.13: Linear regression of the measurement of the angle accuracy of the stepper motor. A linear function $f(x) = p_1 \cdot x + p_0$ was fitted to the data points.

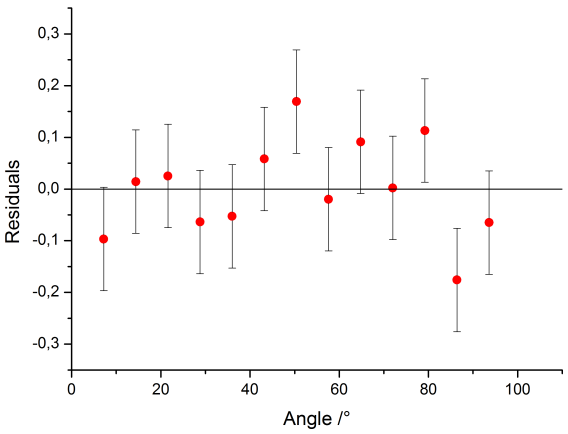

Figure 4.14: Residual plot of the measurement shown on the left.

that the large uncertainty is caused by the diffused border of the light spot on the wall and not obtained by Gaussian error propagation.

4.4.2 Anglular Accuracy of the Stepper Motor

Important for the measurement of the relative PDE is the angle accuracy of the stepper motor of which the manufacturer states it is $\sigma_\Theta = 1.8° \cdot 0.05 = 0.09°$ [16]. For this purpose, a polar plot with the angle interval of the measurement (7.2°, 14.4°, 21.6°, ...) has been created and printed. Secondly, a hex key was attached to the top of the stepper motor instead of the aluminium box. For every measurement, the stepper motor performed 4 steps, which is equal to 7.2°, and the actual position has been read from the printed polar plot with an estimated uncertainty of 0.1°. Afterwards a linear regression was applied to the data. The plot of the measurement and the corresponding residual plot are shown in figure 4.13 and 4.14. The stepper motor did not miss a step and the χ^2/ndf of 0.96 is quite good. Thus an angle uncertainty of $\sigma_\Theta = 0.09°$ will be used in the analysis of the relative photon detection efficiency.

4.4.3 Test for Scattered Light inside the Dark Box

Avoiding scattered light at angles around 90° is very critical due to the correction factor $(1/\cos\Theta)$ in formula 4.10 (page 21). To see whether scattered light exists, a lens mount was covered with felt and put into the optical path while measurements were taken (fig. 4.15). Measurement 1 was taken with the covered lens mount in the middle of the optical path, measurement 2 with the covered lens mount near to the light source. The results, shown in figure 4.15, reveal that all scattered light

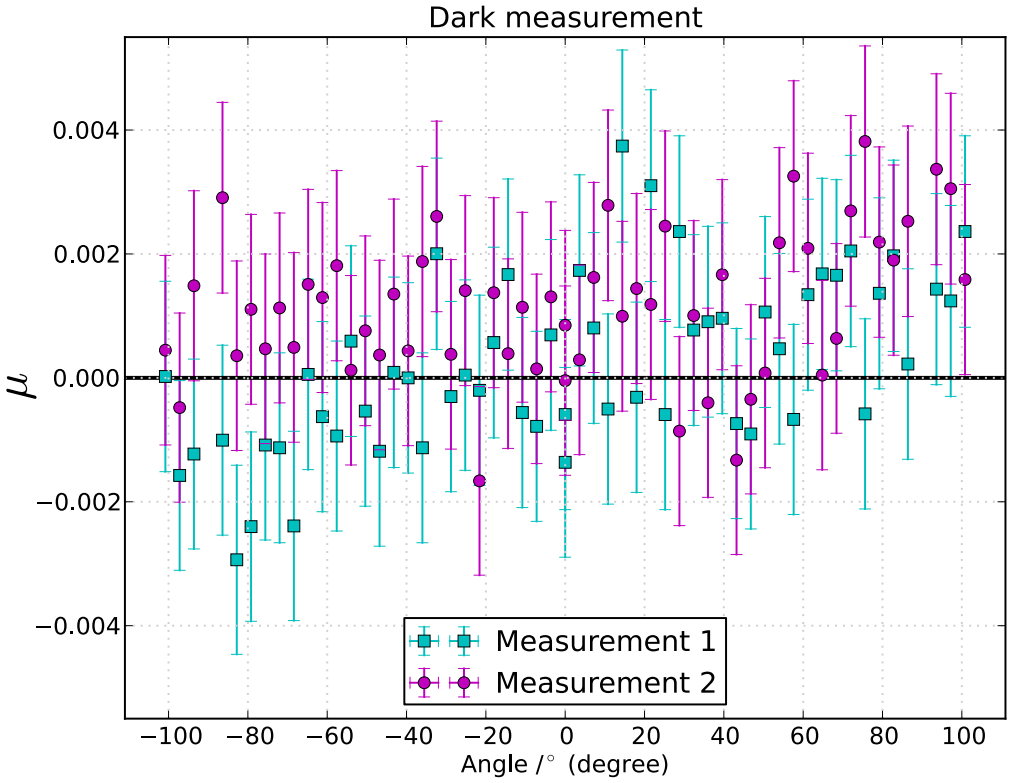

Figure 4.15: Measurement to test for scattered light. **Measurement 1:** Lens mount covered with felt placed in the middle of the optical path. **Measurement 2:** Lens mount right in front of the light source. The amount of detected scattered photons μ (eq. 4.8) is compatible with 0 and does not show strong systematics since χ^2-value of 0.84 for measurement 1 and 1.18 for measurement 2 is quite good.

is compatible with 0 within the uncertainties, thus there is no significant scattered light. The mean number of detected photons was determined by formula 4.8. This is expected since the light is well collimated and the aluminium box is covered with a matt, black varnish to avoid reflections. Additionally, the walls of the dark-box are covered with felt.

It has been proven, that the experimental setup is well adjusted and the slight inhomogeneity of the light spot does not take into account. The next chapter deals with the theory of the behaviour of light when moving between materials with different refractive indices. This is described by the Fresnel equations.

4.5 Fresnel Theory and Monte Carlo Simulations

Due to the resin layer of the SiPM, there is no direct transition between air and silicon for the photons but rather a transition between air and resin and shortly after a transition between resin and silicon. This requires a closer look at the processes inside the SiPM.

The behaviour of light when travelling between two media with different refractive indices n_1, n_2 is described by the Fresnel equations. The light can either be reflected or refracted into the second medium. For the reflected light, the angle of incidence is equal to the exit angle $\Theta_{in} = \Theta_{out}$. If the light is refracted, Snell's law (eq. 4.13) gives the information about the angle of refraction [18](s. 233).

$$\frac{\sin(\Theta_{\text{in}})}{\sin(\Theta_{\text{out}})} = \frac{n_2}{n_1} \tag{4.12}$$

$$\Leftrightarrow \cos(\Theta_{\text{out}}) = \sqrt{1 - \left(\frac{n_1}{n_2} \cdot \sin(\Theta_{\text{in}})\right)} \tag{4.13}$$

To calculate the transmission- and reflection coefficients we have to distinguish between two types of light:

1. s-polarized (from *senkrecht*, German for perpendicular) light.
2. p-polarized (parallel polarized) light.

The reflection coefficients R_s, R_p are given by [18](s. 235)[11]:

$$R_s = \left|\frac{n_1\cos(\Theta_{\text{in}}) - n_2\cos(\Theta_{\text{out}})}{n_1\cos(\Theta_{\text{in}}) + n_2\cos(\Theta_{\text{out}})}\right|^2 = \left|\frac{n_1\cos(\Theta_{\text{in}}) - n_2\sqrt{1 - \left(\frac{n_1}{n_2}\sin(\Theta_{\text{in}})\right)}}{n_1\cos(\Theta_{\text{in}}) + n_2\sqrt{1 - \left(\frac{n_1}{n_2}\sin(\Theta_{\text{in}})\right)}}\right|^2 \tag{4.14}$$

$$R_p = \left|\frac{n_1\cos(\Theta_{\text{out}}) - n_2\cos(\Theta_{\text{in}})}{n_1\cos(\Theta_{\text{out}}) + n_2\cos(\Theta_{\text{in}})}\right|^2 = \left|\frac{n_1\sqrt{1 - \left(\frac{n_1}{n_2}\sin(\Theta_{\text{in}})\right)} - n_2\cos(\Theta_{\text{in}})}{n_1\sqrt{1 - \left(\frac{n_1}{n_2}\sin(\Theta_{\text{in}})\right)} + n_2\cos(\Theta_{\text{in}})}\right|^2 \tag{4.15}$$

If the light is unpolarized, e.g. after being lead into an integrating sphere, the reflection coefficient R can be calculated from:

$$R = \frac{R_s + R_p}{2}. \tag{4.16}$$

And finally, one gets the transmission coefficient T due to energy conservation from:

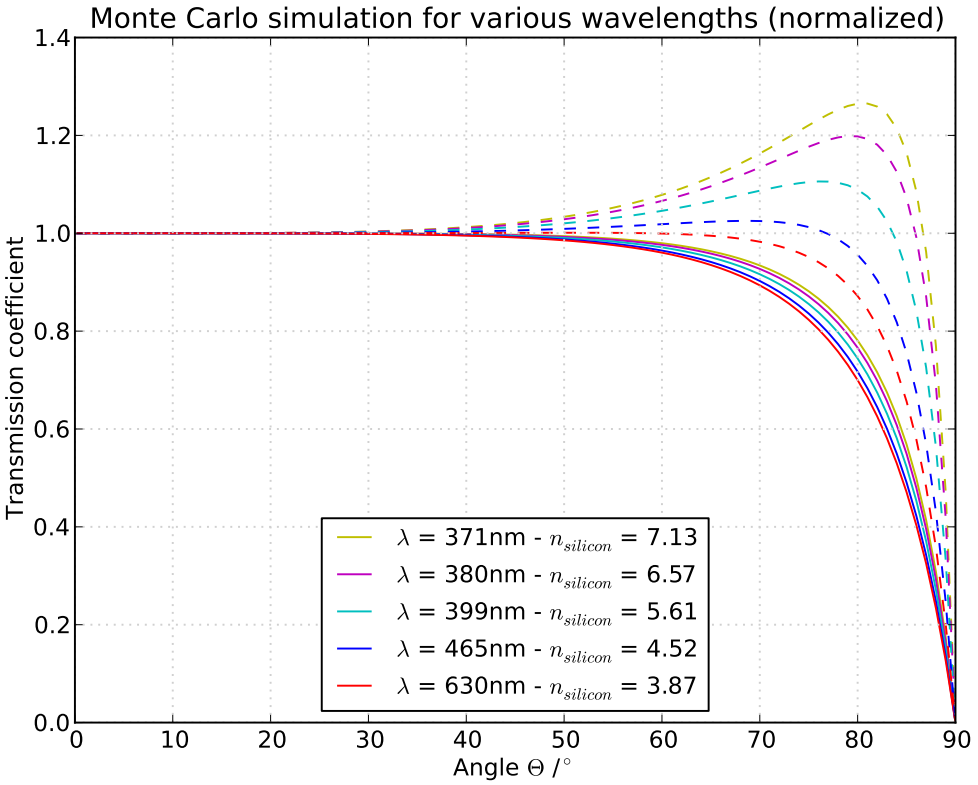

Figure 4.16: Transmission coefficients for various wavelengths normalized to 1 for unpolarized light. Dashed lines represent simulations without, solid lines with multiple reflections

$$T = 1 - R \tag{4.17}$$

The silicon of the SiPM is coated with a layer of resin. The manufacturer of the SiPM states, that the resin, which protects the silicon of the SiPM from oxidation and mechanical damage, has a refractive index of $n_{resin} \approx 1.4$ [12]. Due to the resin, multiple reflection between the resin and the silicon can occur.

Thus, a Monte Carlo simulation has been written that includes this fact. This simulation checks for 1,000,000 *virtual photons* whether they are reflected at the transition of air and resin using the Fresnel equations or not. If not, the next step is to calculate the transmission probability for resin and silicon. Either the photon transmits into the silicon layer and the photon is counted as a hit, or it gets reflected. While the photon is between air and silicon inside the resin layer, multiple reflections are calculated till the photon hits the silicon or leaves the SiPM. It has been assumed that the refractive index of air is $n_{\text{air}} = 1$. The wavelength dependency of the refractive index of air has been assumed to be small and thereby

[11] For last transformation of the equation, Snell's law has been used

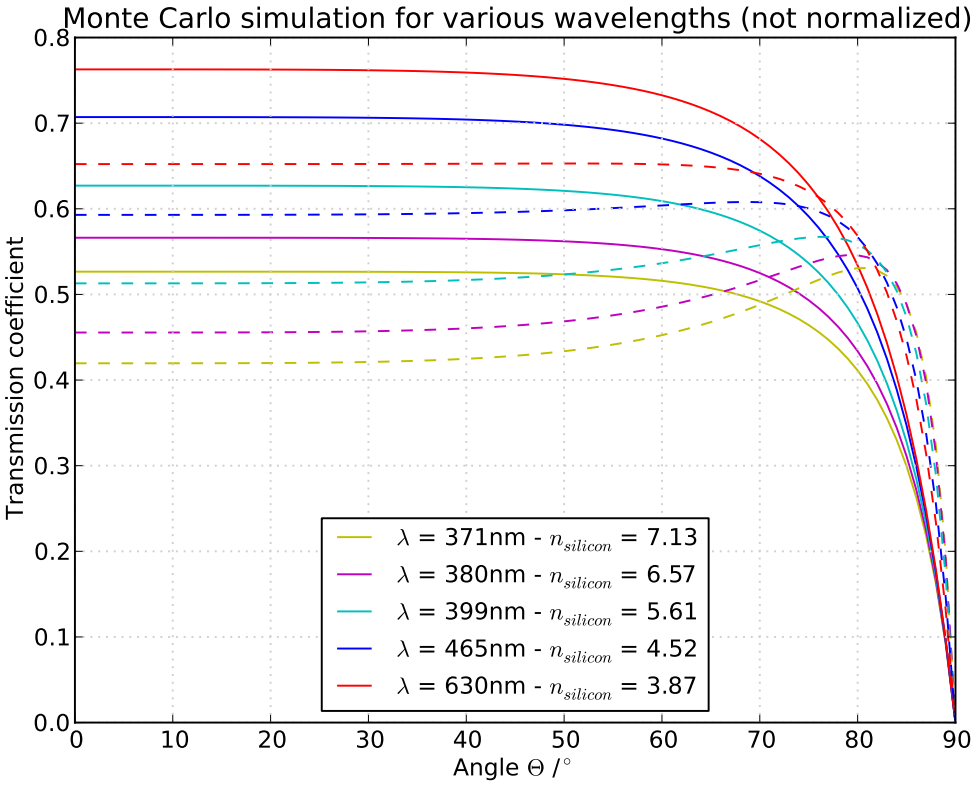

Figure 4.17: Same simulations, but not normalized and also for unpolarized light. Due to the highly transparent resin, the transmission coefficient rises because the angle of incidence on the silicon is smaller.

neglected. Taking a look at the resin, there is no information available about the wavelength dependency and thus, is varied by 0.05 in the further analysis of the relative photon detection efficiency in section 4.6. The refractive index of the silicon is highly wavelength dependent and taken from the website *refractiveindex.info*[12]. The varying refractive indices of silicon for different wavelengths were implemented in the simulation (fig. 4.18). The results of the simulations are shown in figure 4.16 and 4.17. Dashed lines represent simulations without the effects of the resin, solid lines take multiple reflections into account. As one can see on the plot 4.17, the transmission coefficients are higher if a layer of transparent resin with a small refraction index is used. This changes the angle of which the light hits the silicon to a more steep angle. Consequently, the transmission coefficient for the silicon rises.

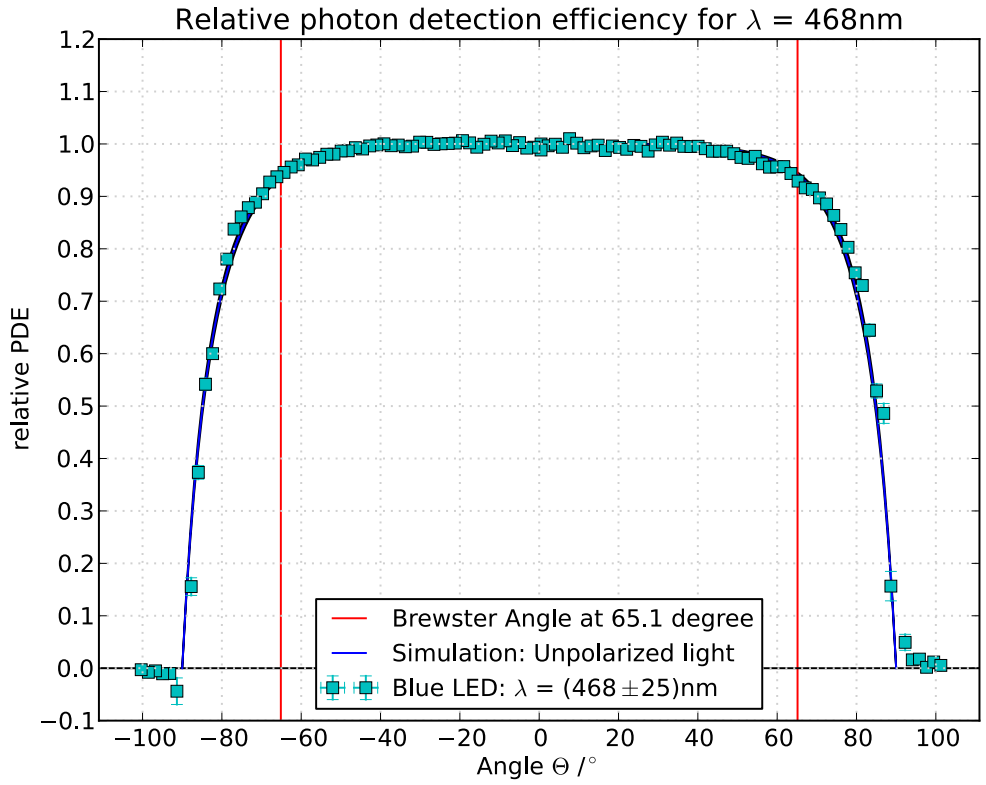

Figure 4.18: Measurement of the relative PDE using an Hamamatsu S103612-11-100C SiPM. An angle correction of $\Phi = 0.46°$ has been applied. One may note that this is exactly the same SiPM used in [12] operated with an overvoltage of $V_{OV} = (1.3 \pm 0.2)$ V.

4.6 Measurements of the Relative Photon Detection Efficiency

4.6.1 SiPM: Hamamatsu S103612-11-100C

The first SiPM used was a Hamamatsu S103612-11-100C which has been used previously for similar measurements in [12]. It is a commercial available SiPM manufactured by Hamamatsu Photonics consisting of a matrix of 10x10 cells covering an area of 1x1 mm^2, so each pixel has a size of 100 x 100 µm. The maximum quantum efficiency, including correlated noise, is stated by the manufacturer to be 65%[13] for a wavelength of $\lambda = 440$ nm [17]. For this reason, all measurements where only one LED is needed are performed with a blue ($\lambda = (465 \pm 22)$ nm) LED. A picture of the SiPM taken with a microscope is shown in figure 4.5 on page 16.

[12] http://refractiveindex.info/?group=CRYSTALS&material=Si - Option SOPRA20
[13] Included are the effects of correlated noise.

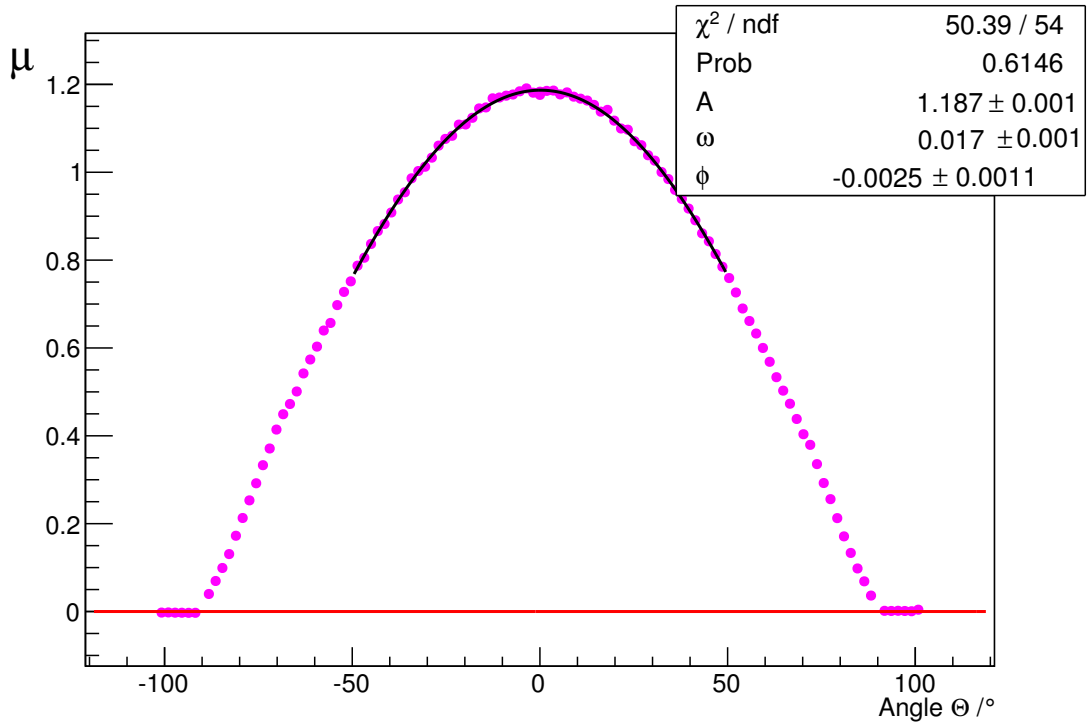

Figure 4.19: Shown is an example of the mean of detected photons μ against the incident angle. The photon flux decreases with increasing angle which is expected. For angles above 90° no photon hits the SiPM anymore.

Based on the analysis described in section 4.3 on page 19 a C++ program has been written to perform an automated analysis of the measurements.

First of all, the QDC spectra and other data such as temperature, operating voltage and angle are read in from the ROOT file created by the measurement-program. Using the class *TSpectrum*, the peaks in the QDC spectrum are located, the middle between the first (pedestal) and second (one p.e.) peak is calculated and used to determine the entries in the pedestal N_{ped} by integrating from bin 0 to the middle of the first and second peak. Every QDC spectrum has got 100,000 entries, which is equal to N_{tot}. Also the statistical uncertainty on the entries in the pedestal is calculated using the statistical Binomial error (eq. 4.6). Furthermore the mean of detected photons μ and its uncertainty is calculated and afterwards the relative PDE according to formula 4.10, too. To calculate the uncertainties of the relative PDE σ_{PDE}, Gaussian distributed random numbers with a mean of $\mu(\Theta)$, $\mu(0)$, and Θ and their uncertainties are created and put into a histogram using formula 4.10. Afterwards, a Gaussian fit is applied returning σ_{PDE} and all data is put into a text file for further processing. Also the operating voltage, mean temperature, the value of the *angle correction*, the minimal and maximal temperature is put into a separate text file. The angle correction factor Φ is described in the next passage.

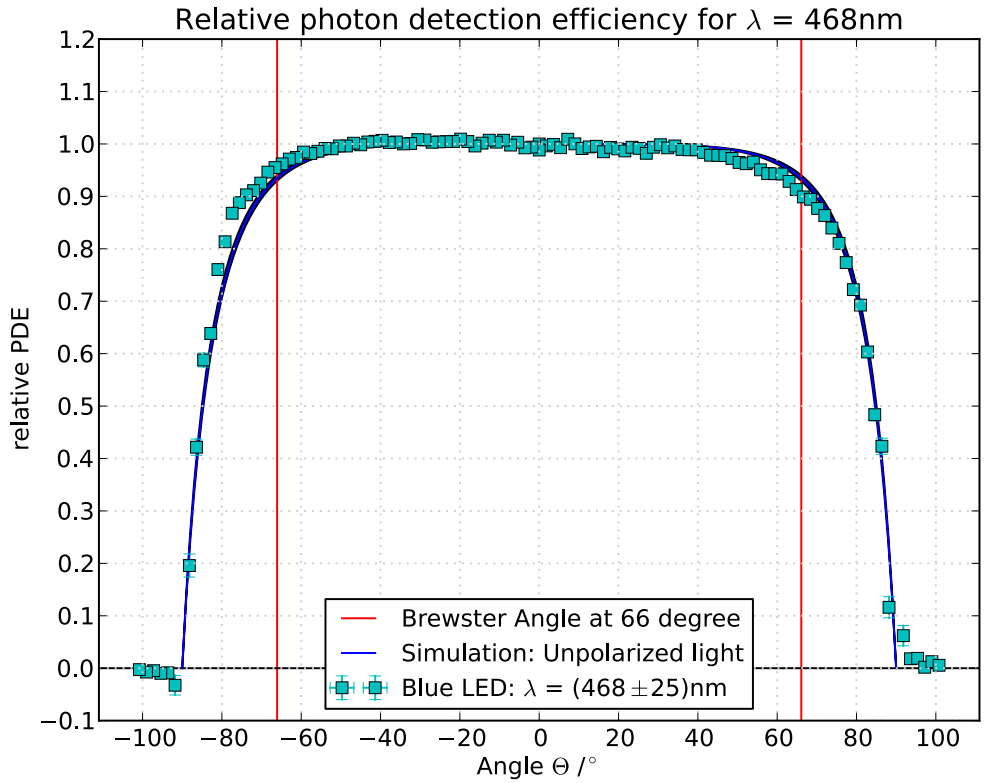

Figure 4.20: Shown is a plot of the same measurement as shown in 4.18 but without an applied angular correction. Clearly visible is the asymmetric trend of the data which can be corrected shifting the data by an correction factor $\Phi = 0.46°$ given by a fit of function 4.18. If a measurement would have been performed in only one direction, the asymmetric trend of the data would be hidden and the relative PDE would be underestimated.

One occurring problem is the adjustment of the aluminium box on the stepper motor. The setup makes a very precise orientation towards the collimated light very difficult. The stepper motor itself can only perform steps of 1.8°, so there is no chance for corrections. Also the plain orientation of the SiPM mounted on the box is not perfect. Beside the measurements which are very symmetric around 0°, there are also measurements which are inclined. These measurements show a shift of the data points as shown in figure 4.20. It has been assumed, that up to an angle of 50° the loss of area is corrected by the factor $1/\cos(\Theta)$ and thus, it is possible to find the offset by fitting a function of the form:

$$f(\Theta) = A \cdot \cos(\omega \cdot \Theta + \Phi) \tag{4.18}$$

to the mean of detected photons μ from $-50°$ to 50° as shown in figure 4.19. This fit is quite good since the $\chi^2/ndf = 0.93$ and returns a angular phase shift of $\Phi = 0.15°$

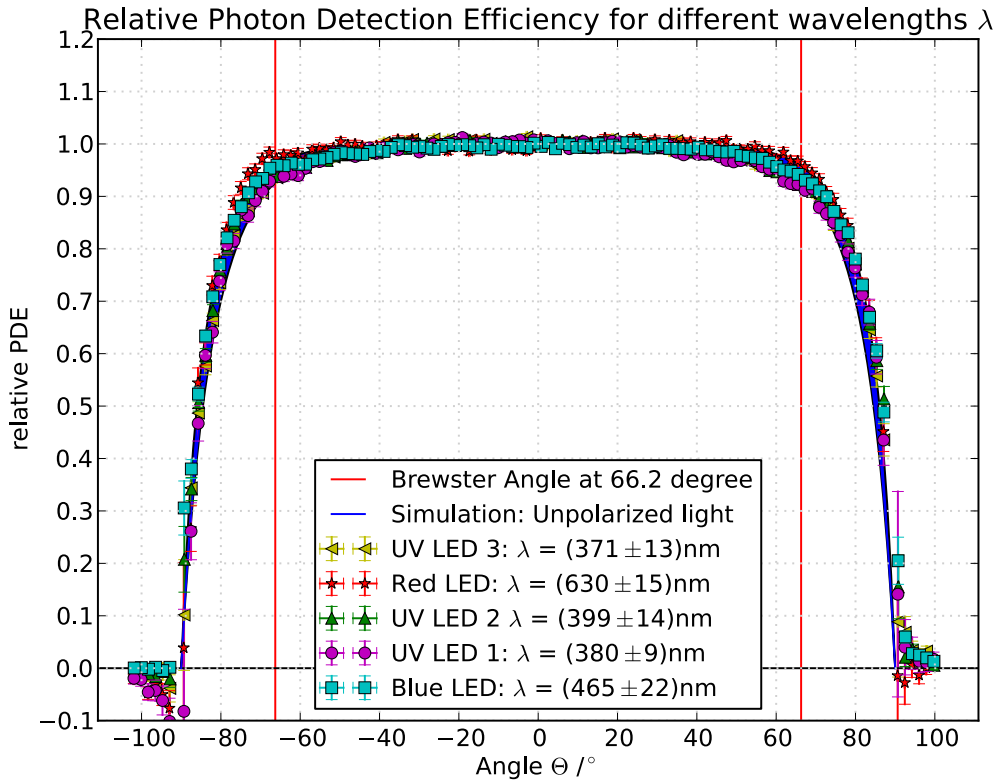

Figure 4.21: Shown are 5 measurements of the relative PDE which is over 90% up to $\Theta \approx 75°$ for different wavelengths. Also the data points show the same behaviour for every wavelength. The data points are in good agreement with the theory given by the Fresnel equations if multiple reflections between the resin and the silicon are taken into account. All measurements were performed with an overvoltage of ≈ 1.3 V

which would be nearly impossible to correct by hand. Consequently, all angles are corrected for this value and the whole analysis described above is applied again to the measured data. An example for an uncorrected measurement is shown in figure 4.20. It represents the same data as shown in figure 4.18 but without the applied correction.

As mentioned before in section 4.5, the refractive index of silicon n_{silicon}, used for the simulation, is especially taken for the given wavelength of the LED (fig. 4.18) and n_{resin} is varied by 0.05 which leads to the illustrated uncertainty region. Also shown is the Brewster angle for the simulation. The Brewster angle is determined by simulating the transmission coefficients at different angles only for parallel polarized light. Afterwards, the maximum of the graph is determined which is by definition the Brewster angle[14].

[14]It is the angle of total reflection for s-polarized light

This measurement has been repeated for several LEDs from UV to red (fig. 4.21) which have been analysed with an fibre spectrometer [19] to obtain the peak emission wavelengths and the spectral widths (FWHM). The specifications of the used LED can be found in the legend of every plot[15]. Due to the correction factor in formula 4.10, the uncertainties around $\Theta = 90°$ are very high ($1/\cos(89°) = 57.3$).

During the measurements of the relative photon detection efficiency, it turned out that if the SiPM is rotated by 90°, the shape of the measured data changes. This is discussed next.

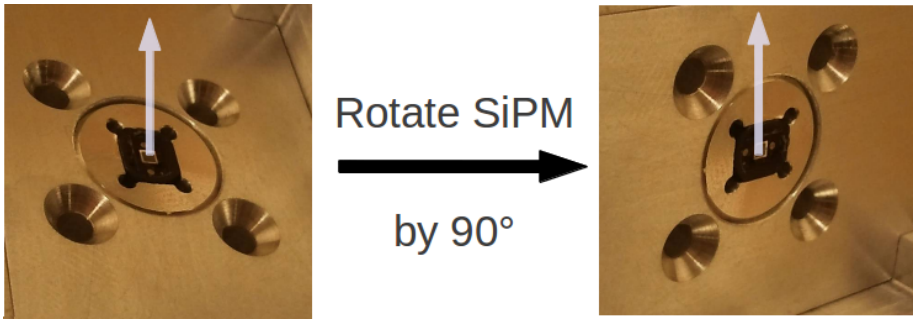

Figure 4.22: Sketch showing how the SiPM is rotated around the illustrated axis.

From now on, the SiPM has been rotated by 90° in a way that the golden contacts are left and right of the sensitive area of the SiPM. One may note that this is still the same SiPM as before (fig. 4.4 and 4.22).

To turn the SiPM on its own axis, it is only necessary to open the aluminium box, turn the mount of the SiPM and close the aluminium box. Thus nothing else has been changed, even not the connection between the stepper motor and the aluminium box.

Surprisingly, the shape of the measured data has changed as shown in figure 4.24 and is not described by the theory any more. The photon detection efficiency is constant equal to ≈ 1 up to 60° rises slightly and then drops to a local minimum[16]. After another small rise, the curve drops rapidly to zero. To illustrate this, the relevant data, shown in figure 4.23, has been summarized in table A.1 in the appendix.

Another interesting characteristic can be seen in figure 4.24 where the relative photon detection efficiency is shown for LEDs with various wavelength. In comparison with the theory, shown in plot 4.16 and 4.17, the relative photon detection efficiency for red light should be the observed minimum, but is the highest. This has been also observed at measurements performed before, which are shown in the appendix (fig. A.1 on page 47).

[15] More plots of the relative photon detection efficiency can be found in the appendix.

[16] This has been seen in various measurements, one illustrating plot is shown in the appendix (fig. A.1).

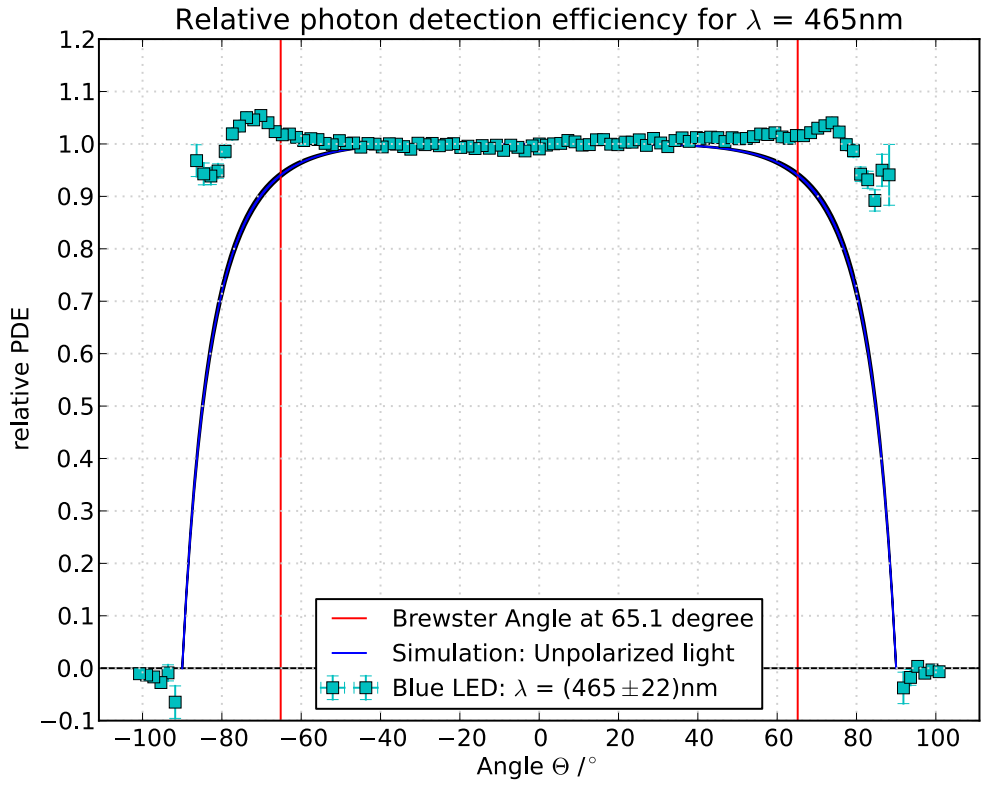

Figure 4.23: Measurement of the relative PDE after rotating the SiPM by 90° (the golden contacts of the SiPM are now left and right of the light sensitive area of the SiPM).

This phenomenon was not observed by J. Schumacher [12], in this work, however, only measurements with the contacts of the SiPM located along the rotating axis were performed. To figure out, why the shape of the measurement changes if the SiPM is rotated, a measurement with the SiPM at 45° has been performed. This means, the golden contacts of the SiPM are pointing to the upper left and lower right corner[17]. This third measurement reveals that the shape of the measurement changed to a mixture of the two extrema discussed before (fig 4.25).

Apparently, the shape of the measurements change depending on the position of the golden contacts of the SiPM which provide the bias voltage. A possible explanation is shown in figure 4.26[18], 4.27 and 4.28. Shown is a sketch of the cross section of an SiPM. There are two main regions, the golden contact with a width of 0.1 mm and the

[17] The rotating axis points vertically upwards

[18] n = refractive index of the resin
cw = width of the contact
α = angle of incidence
h = thickness of the resin

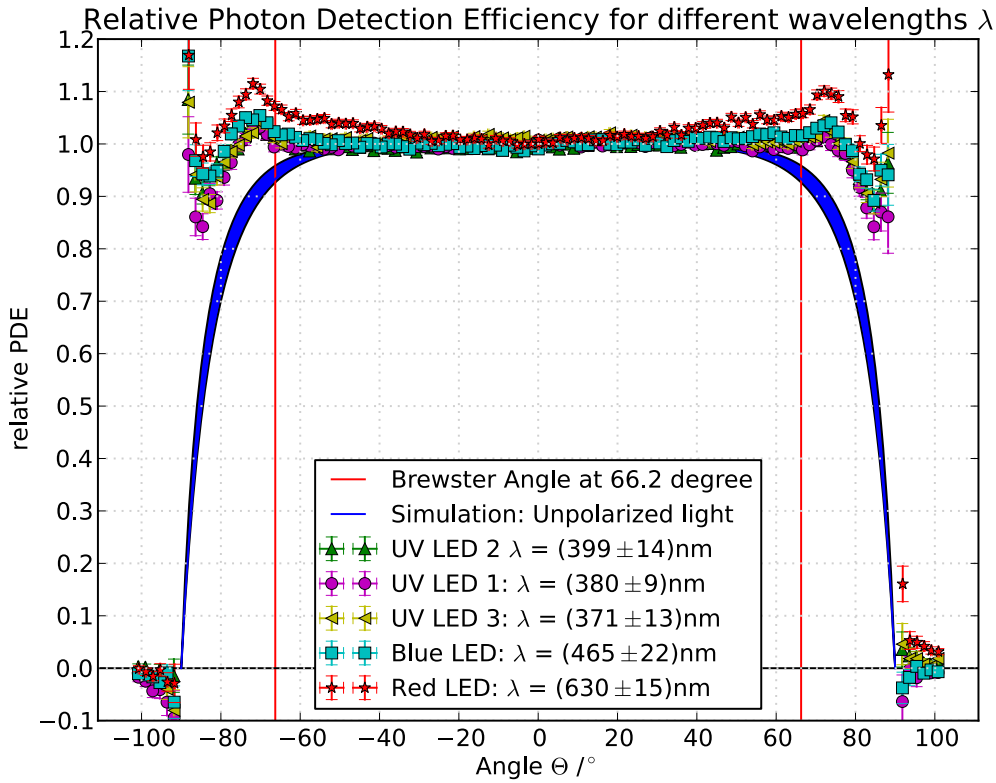

Figure 4.24: Shown in this plot is a measurement of the relative PDE after the SiPM has been rotated. The golden contacts are left and right of the sensitive area of the SiPM. As one can see, the shape of the measured data has changed and does not follow the prediction given by the Fresnel equations. A possible explanation is discussed in the text. The uncertainty region shown, is given by simulating the transmission coefficient for the used wavelengths and thus, for various refractive indices of the silicon.

photon sensitive area of the SiPM. Of course, the SiPM is completely illuminated but for the moment, only the fraction of light which hits the golden contact is important.

The light hits the resin in an angle of $\alpha = 62°$ and gets refracted due to the different refractive indices of air ($n_{air} \approx 1$) and the resin ($n_{resin} \approx 1.4$). After the refraction, the light is being reflected at the golden contact and reflected again at the upper side of the resin and can hit the sensitive area of the SiPM. The dimensions of the SiPM have been taken from the constructional drawing by Hamamatsu Photonics [17]. The sensitive area of the SiPM has a length of 1 mm, the distance between the contact and the SiPM is also 1 mm. The height of the resin has been approximated to $h = 0.6$ mm.

On the one hand, this is a possible explanation why the Fresnel equations describe accurately the measured data if the golden contacts can not reflect any light towards the sensitive area of the SiPM, since they are located along the rotating axis underneath and above the sensitive area. On the other hand, it is an explanation why the

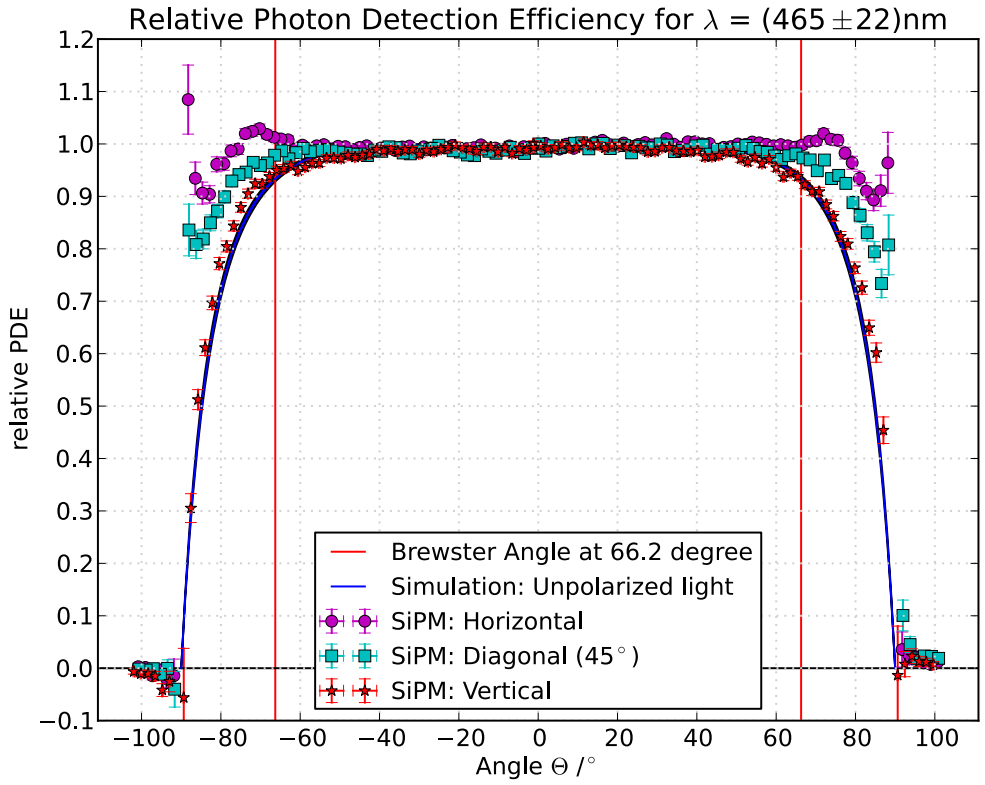

Figure 4.25: Comparison of the relative PDE at different positions of the SiPM. It looks as if the vertical and horizontal positions of the SiPM lead to the most extreme results. The measurement done at 45° seems to be a mixture of both.

shape of the data changes if the SiPM is rotated. At an angle of 72° the total beam reflected by the contact hits the SiPM in theory (fig. 4.27) where also is the maximum of the relative photon detection efficiency (fig. 4.23 and 4.24). The maxima of the measured photon detection efficiency for the measurements shown in figure 4.24 are at angles of $(71.96° \pm 1.8°)$, $(72.02° \pm 1.8°)$, $(72.01° \pm 1.8°)$, $(73.83° \pm 1.8°)$ and $(72.11° \pm 1.8°)$. Figure 4.28 shows the simulation for an incident angle of 82° where still no reflected light falls outside of the sensitive area of the SiPM. Thus, there is no decrease of the relative photon detection efficiency up to angles of 90°. If the SiPM is rotated by its own axis to 45°, there is a smaller amount of the reflected light which is reflected onto the sensitive area. In addition, the golden contacts do not seem to be polished, therefore the light could be reflected diffuse which leads to more light than expected at even lower angles.

This leads to the conclusion that the relative photon detection efficiency measured while the golden contacts being underneath and above the sensitive area of the SiPM is the one without significant disturbances. Another difficulty is the surface of the resin of the SiPM. The Fresnel equations assume a perfectly plane surface but the surface of an SiPM is wavy due to the construction process, but since the Fresnel equations can describe the trend of the data, this might be of less importance.

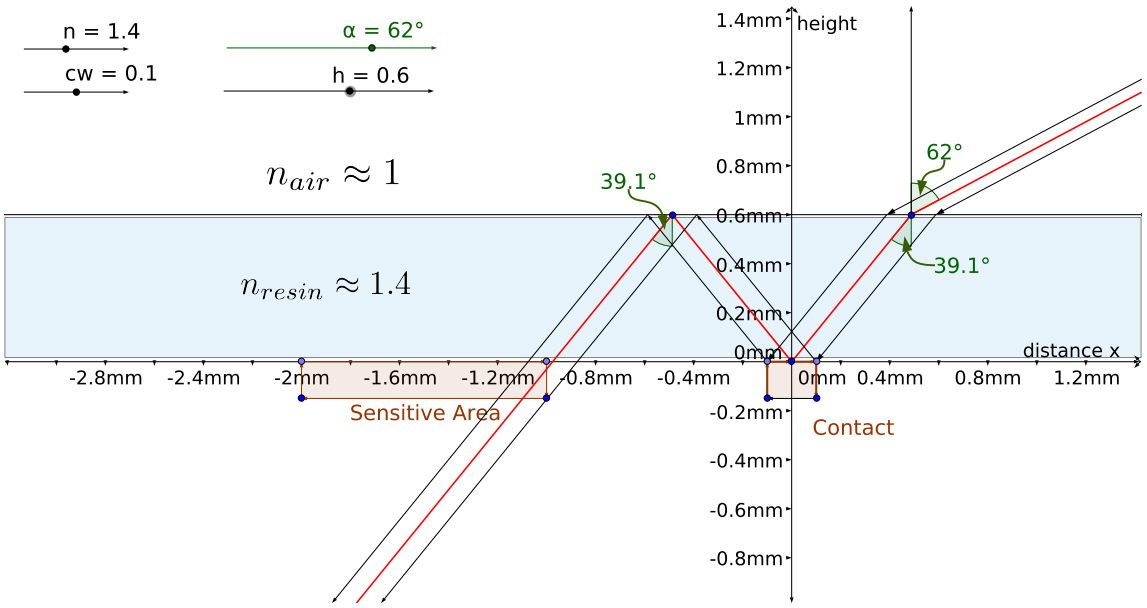

Figure 4.26: Shown is a sketch of a cross section of an SiPM. The light hits the resin on the right in an angle of $\alpha = 62°$, gets refracted and gets reflected at the golden contact at (0,0). After another reflection at the surface of the resin, the light hits the sensitive area of the SiPM. This leads to an additional amount of light which is not described by the Fresnel equations as seen in figure 4.23 and 4.24.

Nevertheless, this does not change the potential of the usage of SiPM for the detection of fluorescence light. With regard to FAMOUS, the golden contacts of the SiPM will be covered by the Winston cones, thus no light can be reflected by the contacts onto the sensitive area. Since the relative photon detection efficiency is over 90% up to angles $\Theta = 75°$ the use of Winston cones as light funnels will not significantly decrease the efficiency of the system of Winston cone and SiPM. One upcoming question is, whether the relative photon detection efficiency changes if an SiPM with different pitch is used. This is discussed in the next chapter.

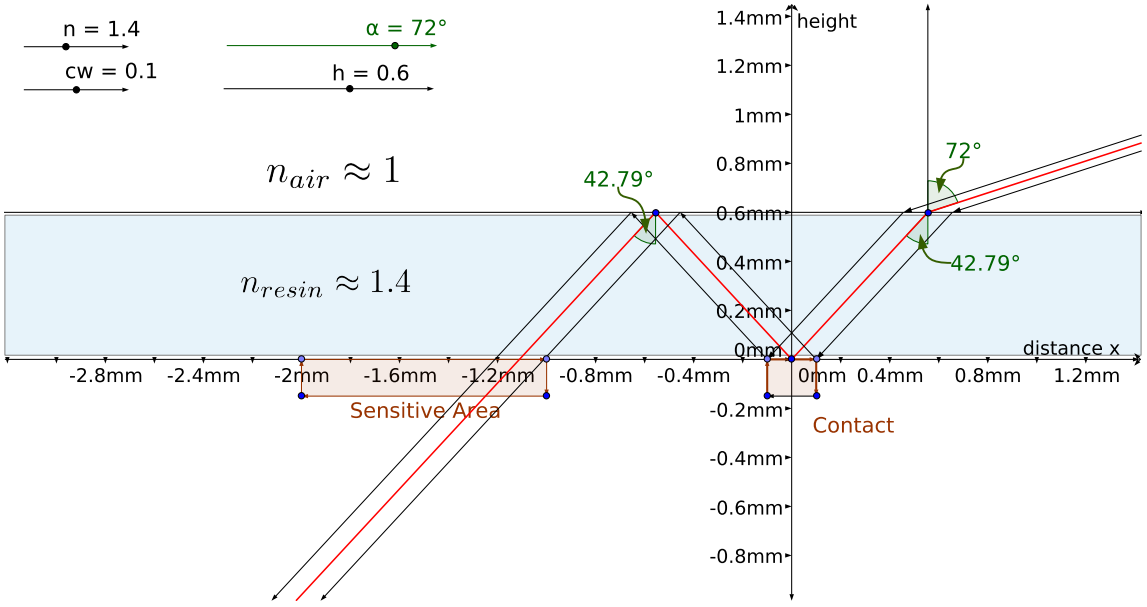

Figure 4.27: Shown is the same sketch as shown in figure 4.26 but the incident angle of light is set to 72°. The complete reflected beam hits now the SiPM which results in a maximum of the relative Photon Detection Efficiency (fig. 4.23 and 4.24).

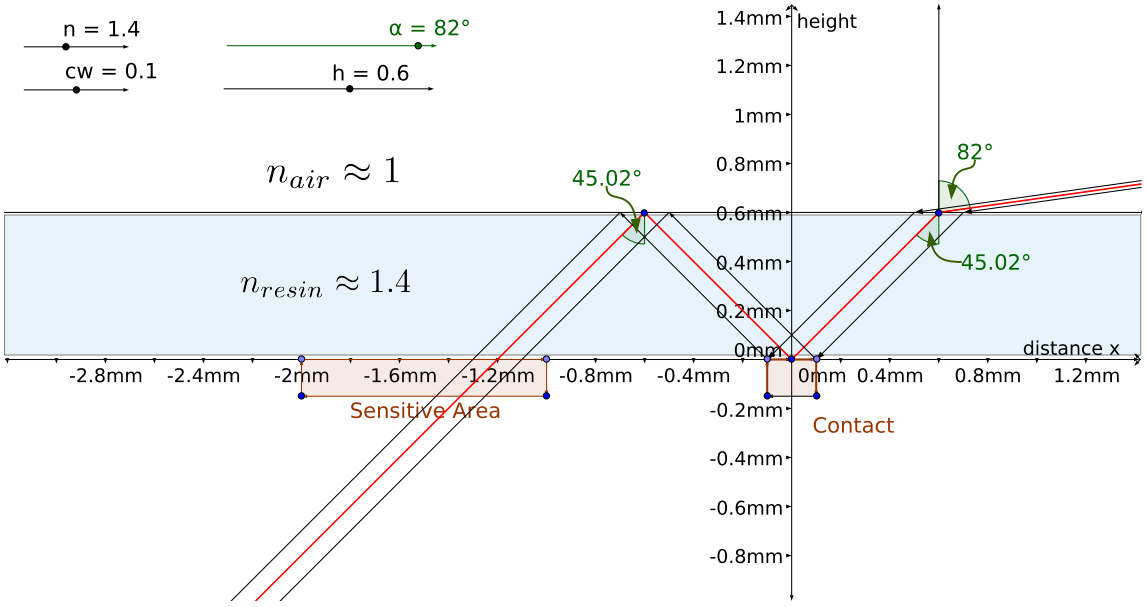

Figure 4.28: Shown is the same sketch as shown in figure 4.26 but the incident angle of light is set to 82°. As one can see, no light falls outside of the sensitive area of the SiPM. It is also possible to change the height of the resin, the refractive index of the resin and the width of the golden contact to simulate several scenarios.

4.6.2 SiPM with 50 µm pitch

This chapter deals with the relative photon detection efficiency at different incident angles for an 1x1 mm^2 SiPM with a pixel size of 50 µm, which is also called the pitch of an SiPM. It is not expected that anything will change, since the basic build-up of the used 50 µm SiPM is similar to the one used before. Only the pitch is different. The setup has not been changed, only the SiPM has been replaced and also the same LEDs have been used. SiPMs with a smaller pitch have a lower noise rate due to the smaller sensitive area. This leads to nicer QDC spectra and therefore smaller statistical uncertainties.

Unfortunately, the SiPM was not in its original packaging, so the exact serial number is unknown. This is not very important, since its known, that this is an SiPM with 50 µm pitch and is designed similar, thus all of the theoretical assumptions made before[19] are also valid for this SiPM.

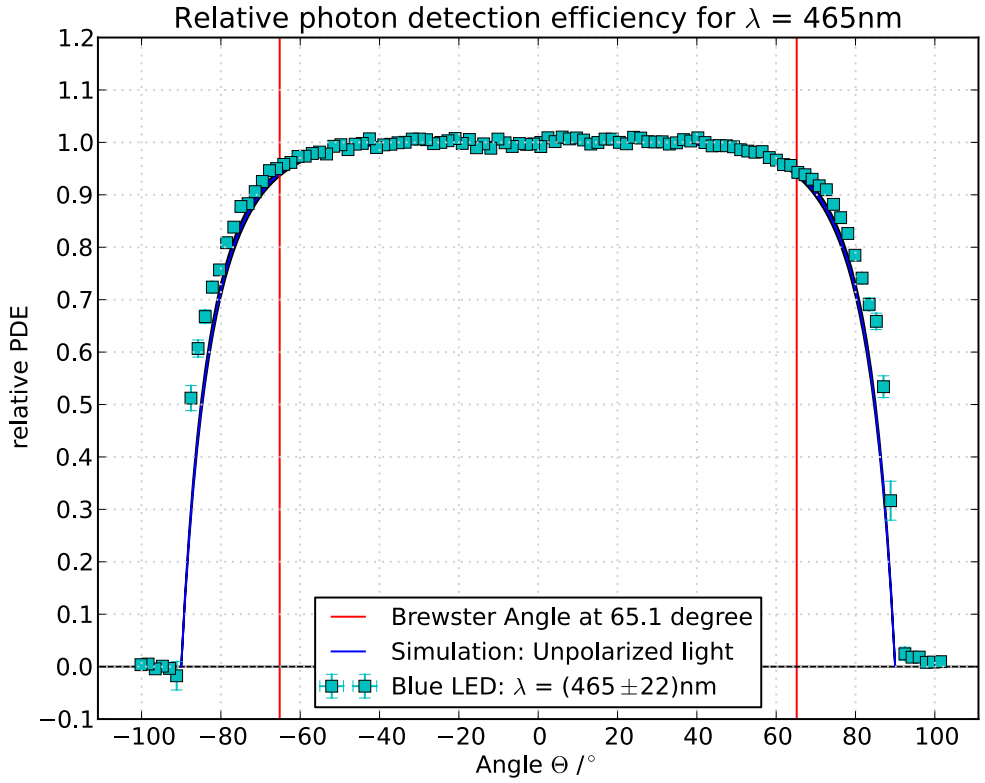

Figure 4.29: Measurement of the relative photon detection efficiency using an SiPM with 50 µm pitch. The overvoltage was set to (1.3 ± 0.1) V and an angle correction of 0.65° has been applied.

The measurement for a blue LED while the golden points were pointing up- and downwards is shown in figure 4.29. As before, the Fresnel equations describe the

[19] Position of the golden contacts, thickness and refractive index of the resin

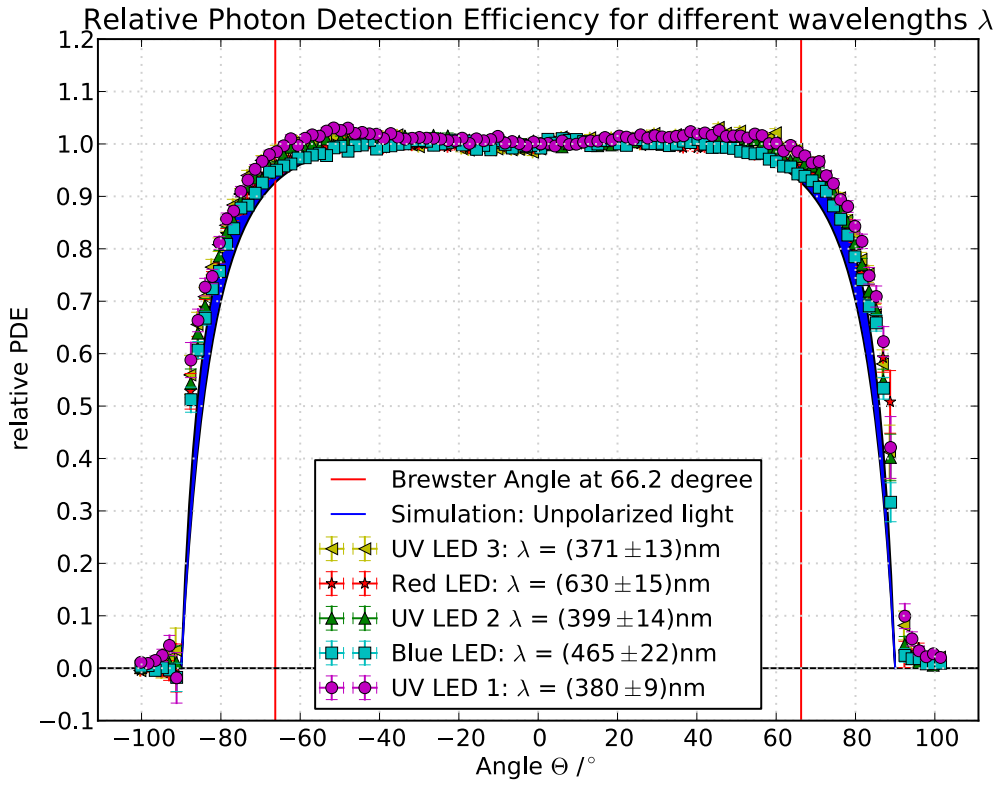

Figure 4.30: Shown are 5 measurements of the relative PDE for an SiPM with 50 μm pitch. Similar to the 100 µm SiPM, the relative PDE is over 90% up to an angle of $\Theta \approx 75°$ for different wavelengths but is a little bit higher than achieved using the 100 µm SiPM.

trend of the data points but in comparison to the 100 µm SiPM, the relative photon detection efficiency is a little bit higher than expected by the theory.

Taking a look at the plot presenting all wavelengths measured shown in figure 4.30, one can see that all measurements show a slight higher trend than expected.

Again as before, the 50 µm SiPM has been turned by 90°, so that the golden contacts are left and right of the sensitive area of the SiPM (fig. 4.22 on page 33). The result is shown in figure 4.31. Similar to the 100 µm SiPM, the shape of the measured data has changed which is discussed detailed in the previous chapter on page 33ff. Thus, there is no effect on the relative photon detection efficiency caused by the pitch of the SiPM.

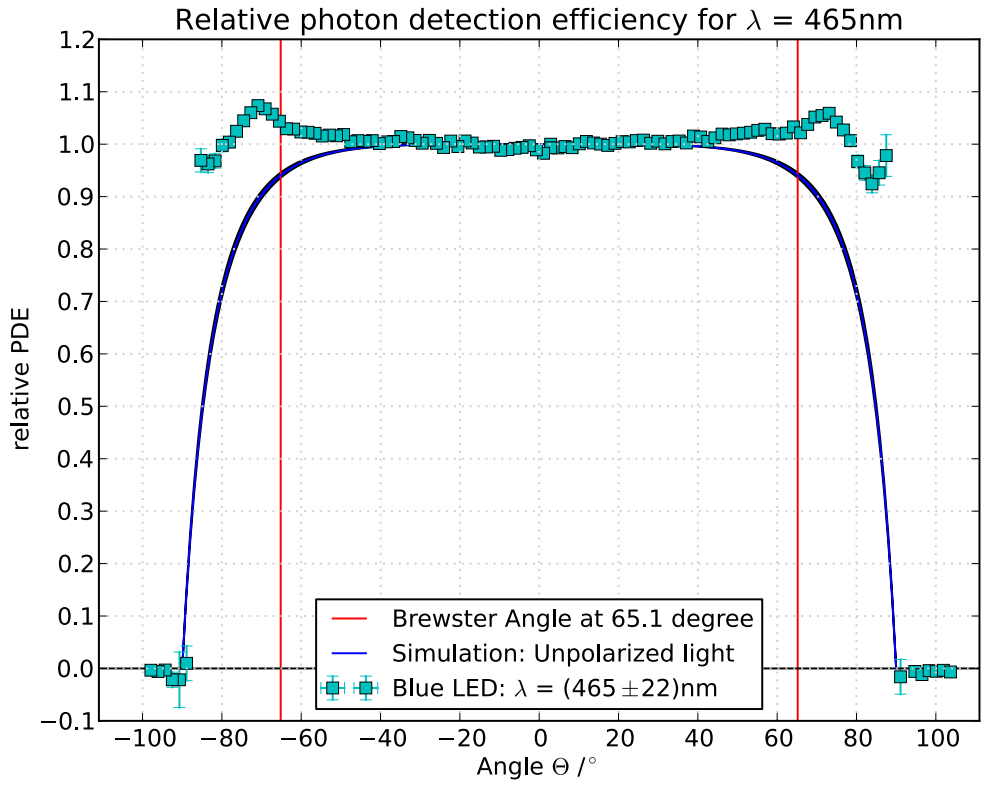

Figure 4.31: Shown is a measurement of the relative photon detection at different incident angles using a 50 µm SiPM. The golden contacts are left and right of the sensitive area. In comparison to a measurement where the golden contacts are underneath and above the sensitive area of the SiPM, the shape of the measurement has changed. A possible explanation is shown on page 33.

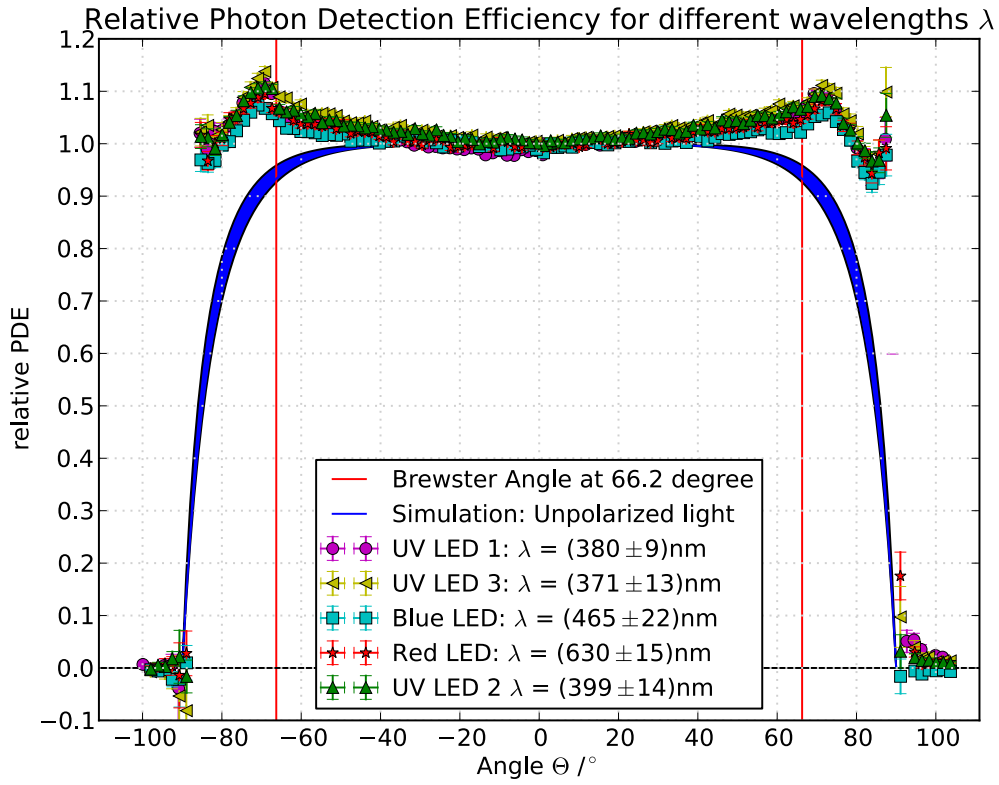

Figure 4.32: Shown in this plot is a measurement of the relative PDE with the 50 µm SiPM rotated. All measurements show the same trend. A possible explanation is shown on page 33.

5. Summary and Outlook

The First Auger Multi pixel photon counter camera for the Observation of Ultra-high-energy cosmic ray Showers (FAMOUS) is a prototype for an SiPM based fluorescence telescope using Winston cones as light funnels. These Winston cones are non imaging devices with a wide range of exit angles, which are used to concentrate the incoming light on a system of silicon photomultipliers to detect the fluorescence light of extensive air showers. To simulate the overall performance of FAMOUS, the angular dependence of the relative photon detection efficiency of silicon photomultipliers must be known.

This thesis has shown, that the relative photon detection efficiency is above 90% up to angles of 75° for various wavelengths from the UV range (371 nm) to red light (630 nm). This can be described by the Fresnel equations if multiple reflections between the resin and the silicon of the SiPM are taken into account and was realized in a self written Monte Carlo simulation. For the measurement of the relative photon detection efficiency, a measurement setup was designed which makes fully automatic measurements possible. Throughout this thesis, there has been performed measurements for 5 different wavelengths and two SiPMs in different orientations. The measured data fits well to the theory given by the Monte Carlo simulation using the Fresnel equations.

During the progress of this thesis, a phenomenon occurred which was not seen before. The silicon photomultiplier was mounted turned by 90°, which resulted in a change of the shape of the measured data. Thus, the data was not following the prediction, given by the Fresnel equations, anymore. Taking a closer look to the design of the used silicon photomultiplier, a possible explanation has been found. Due to the golden contacts providing the bias voltage for the SiPM, light can be reflected at the golden contact and hits the sensitive area of the SiPM. To support this theory, a measurement was performed while the SiPM was mounted at 45°. The shape of the measurement changed to a mixture of both extrema which was expected.

Since the Winston cones used for FAMOUS are of round shape, the golden contacts of the SiPM are covered by the Winston cones, thus this feature will not be seen by FAMOUS. In this case, the relative photon detection efficiency is described by the Fresnel equations as confirmed by the measurements in this thesis over a wide range of wavelengths.

The prototype of FAMOUS is currently in construction. A small prototype of the focal plane with 7 pixels has been constructed by the workshop and a Fresnel lens has been acquired, too. Simulations show that the overall performance of FAMOUS will

be slightly better than the performance achieved at the Pierre Auger Observatory at the moment. The improvement of SiPMs is going fast, new prototypes promising absolute photon detection efficiencies of about 60% and a significant improvement of the fluorescence detection technique.

References

[1] J. Bluemer, R. Engel, and J. R. Hoerandel, *Cosmic rays from the knee to the highest energies*, Progress in Particle and Nuclear Physics, 63 (2009), pp. 293 – 338. Available online http://www.sciencedirect.com/science/article/pii/S0146641009000362, visited 13.09.2012.

[2] J. Beringer et al. (Particle Data Group),*Phys. Rev. D86, 010001*, 2012 Available online http://pdg.lbl.gov/2012/figures/figures.html, visited 13.09.2012.

[3] O. Pooth, *Experimentalphysik V - Einführung in die Teilchen- und Astroteilchenphysik*, III Phys. Inst, RWTH Aachen, WS 2011/2012.

[4] The Pierre Auger Collaboration, *The Cosmic Ray Energy Spectrum and Related Measurements*, 2011 Available online http://arxiv.org/pdf/1107.4809v1.pdf, visited 13.09.2012.

[5] The Pierre Auger Collaboration, *The Pierre Auger Observatory V: Enhancements*, 2011 Available online http://arxiv.org/pdf/1107.4807v1.pdf, visited 13.09.2012.

[6] *Website of the Pierre Auger Observatory*, www.auger.de/.

[7] M. Lauscher, *Characterisation Studies of Silicon Photomultipliers for the Detection of Fluorescence Light from Extensive Air Showers*, master thesis, III. Phys. Inst. A, RWTH Aachen University, 2012

[8] P. Eckert *et al.*, *Characterisation studies of silicon photomultipliers*, Nuclear Instruments and Methods in Physics Research Section A: Accelerators, Spectrometers, Detectors and Associated Equipment, 620 (2010), p. 11. Available online http://arxiv.org/abs/1003.6071, visited 13.09.2012.

[9] B.Dolgoshein, et al., *Nuclear Instruments & Methods In Physics Research Section A*, doi:10.1016/j.nima.2011.12.024, 2011.

[10] T. Niggemann, *New Telescope Design with Silicon Photomultipliers for Fluorescence Light Detection of Extensive Air Showers*, master thesis, III. Phys. Inst. A, RWTH Aachen University, 2012.

[11] M. Lauscher et al., *FAMOUS: A prototype silicon-photomultiplier telescope for the fluorescence detection of ultra-high-energy cosmic rays*, SPIE, 8460-56 (2012)

[12] J. Schumacher, *Characterization Studies of Silicon Photomultipliers: Noise and Relative Photon Detection Eficiency*, bachelor thesis, III. Phys. Inst. A, RWTH Aachen University, 2011.

[13] D. Renker and E. Lorenz, *Advances in solid state photon detectors*, Journal of Instrumentation, 4 (2009), p. P04004. Available online http://stacks.iop.org/1748-0221/4/i=04/a=P04004, visited 13.09.2012.

[14] A. N. Otte, *Observation of VHE Gamma-Rays from the Vicinity of magnetized Neutron Stars and Development of new Photon-Detectors for Future Ground based Gamma-Ray Detectors*, phd thesis, Technische Universitaet Muenchen, Muenchen, 2007.

[15] S. Mann, *Measurement of the UV Reflectivity of Aluminium in Different Stages of Oxidation*, bachelor thesis, III. Phys. Inst. A, RWTH Aachen University, to be published 2012.

[16] *Specification Sheet: RB-Soy-22 (stepper motor)*, Available online http://www.robotshop.com/ca/content/PDF/specifications-sy35st28-0504a.pdf, visited 13.09.2012.

[17] *Specification Sheet: Hamamatsu MPPC Technical Information*, Available online http://sales.hamamatsu.com/assets/pdf/parts_S/high_resolution_mppc_kapd0002e08.pdf, visited 13.09.2012.

[18] W. Demtröder, *Experimentalphysik, Bd.2 - Elektrizität und Optik*, Springer, 1999.

[19] Ocean Optics, *USB2000 - Fiber Optic Spectrometer: Installation and Operation Manual* Available online http://www.oceanoptics.com/technical/usb2000%20operating%20instructions.pdf, visited 13.09.2012.

A. Appendix

A.1 Plots: Hamamatsu S103612-11-100C

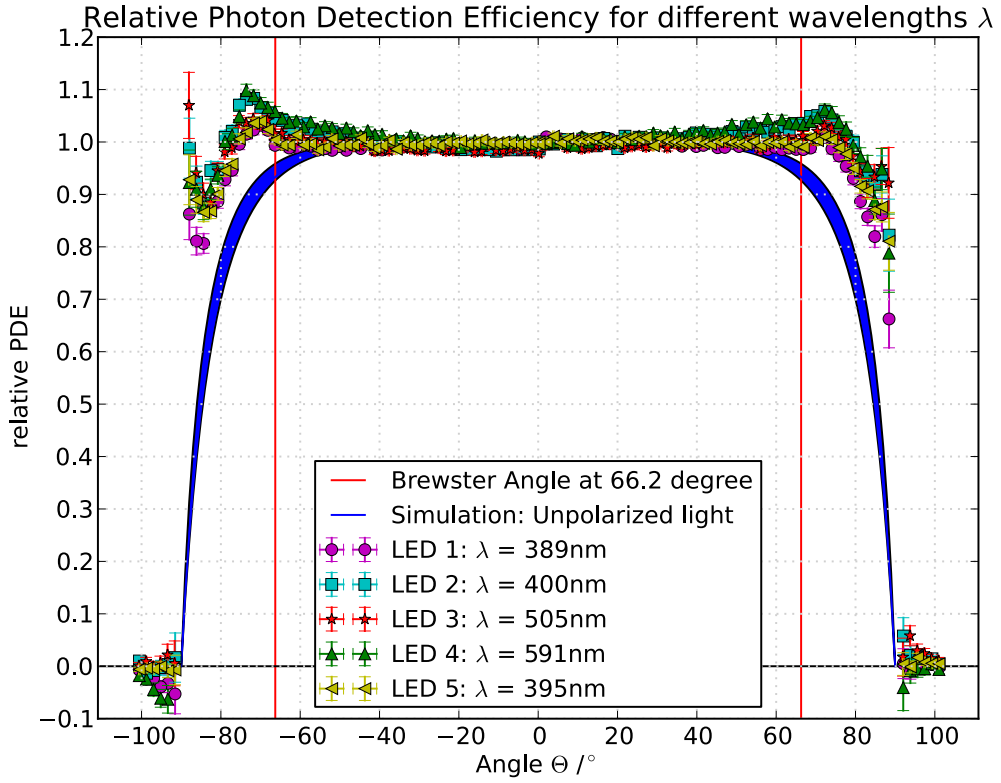

Figure A.1: Measurement of the relative PDE performed earlier for other wavelengths. The longest wavelength got the highest relative PDE which is not predicted by the Fresnel equations. For further information see section 4.5.

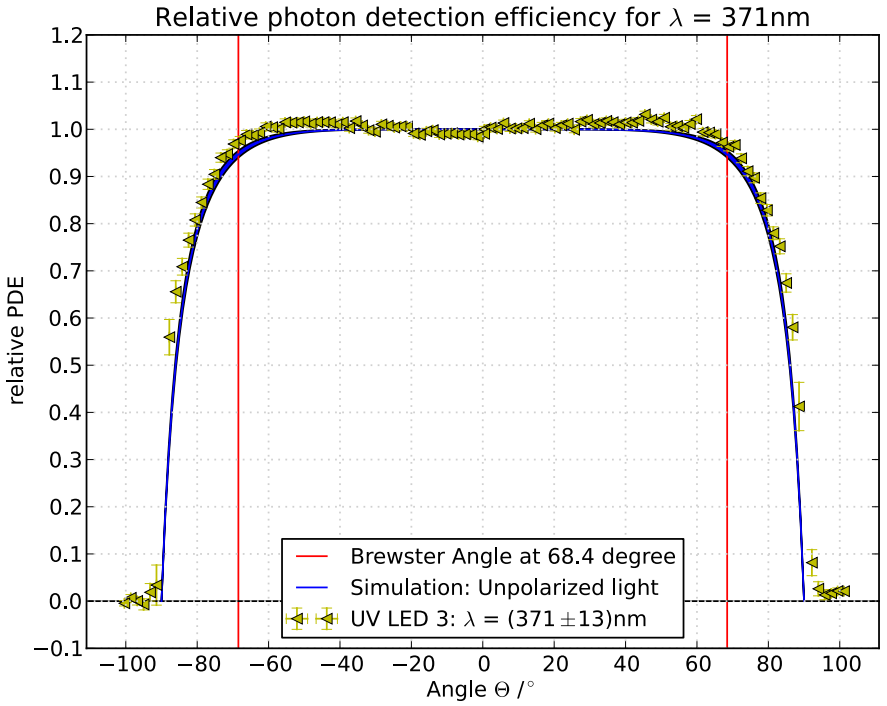

Figure A.2: Measurement of the relative PDE for an LED with $\lambda = 371$ nm.

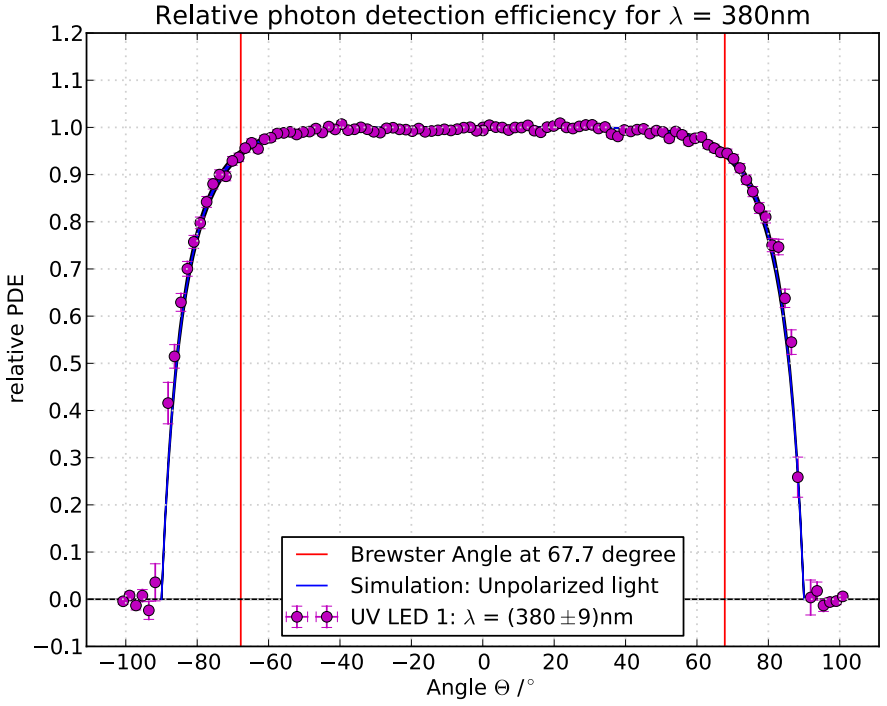

Figure A.3: Measurement of the relative PDE for an LED with $\lambda = 380$ nm.

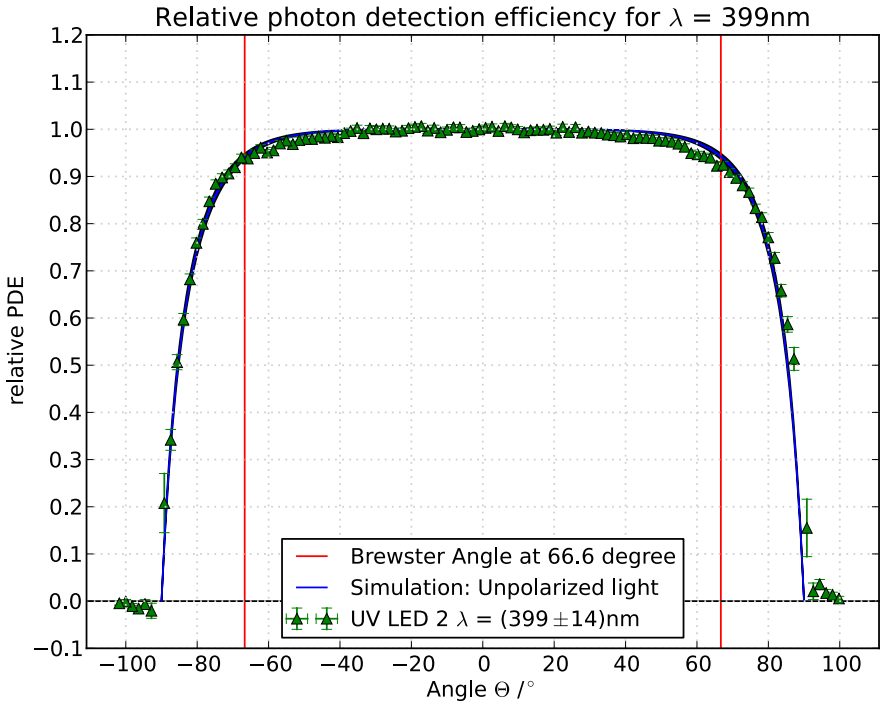

Figure A.4: Measurement of the relative PDE for an LED with $\lambda = 399$ nm.

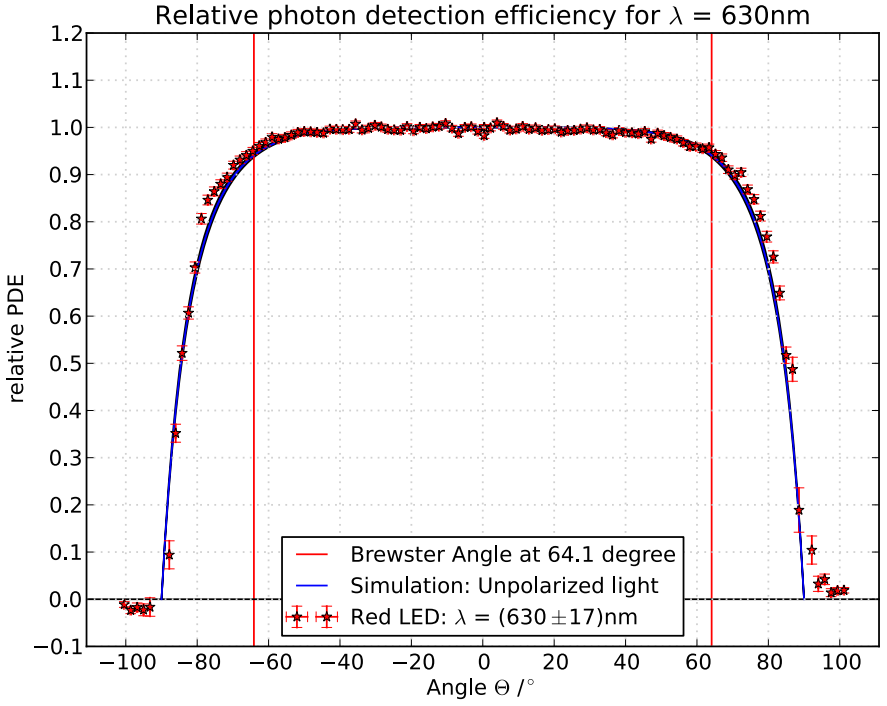

Figure A.5: Measurement of the relative PDE for an LED with $\lambda = 630$ nm.

A.2 Tables

Measurement for positive angles			
Angle /°	σ_{Angle} /°	relative PDE	$\sigma_{\text{rel. PDE}}$
70.2	0.09	1.030	0.009
72.0	0.09	1.035	0.009
73.8	0.09	1.040	0.010
75.6	0.09	1.023	0.010
77.4	0.09	0.999	0.011
79.2	0.09	0.987	0.012
81.0	0.09	0.942	0.014
82.8	0.09	0.932	0.016
84.6	0.09	0.892	0.020
86.4	0.09	0.950	0.030
88.2	0.09	0.941	0.058
91.8	0.09	−0.038	0.030
93.6	0.09	−0.018	0.015
95.4	0.09	0.004	0.010
97.2	0.09	−0.010	0.008
99.0	0.09	−0.003	0.006
100.8	0.09	−0.007	0.005
Measurement for negative angles			
Angle /°	σ_{Angle} /°	relative PDE	$\sigma_{\text{rel. PDE}}$
−70.2	0.09	1.054	0.009
−72.0	0.09	1.046	0.009
−73.8	0.09	1.050	0.010
−75.6	0.09	1.034	0.010
−77.4	0.09	1.019	0.011
−79.2	0.09	0.986	0.012
−81.0	0.09	0.948	0.014
−82.8	0.09	0.939	0.016
−84.6	0.09	0.943	0.021
−86.4	0.09	0.968	0.030
−88.2	0.09	1.168	0.066
−91.8	0.09	−0.065	0.031
−93.6	0.09	−0.009	0.015
−95.4	0.09	−0.027	0.010
−97.2	0.09	−0.017	0.008
−99.0	0.09	−0.013	0.006
−100.8	0.09	−0.011	0.005

Table A.1: Table of the data shown in plot 4.23 on page 34. Right after 90° the relative PDE drops rapidly to ≈ 0.

Danksagungen - Acknowledgements

Hiermit möchte ich mich bei all denen bedanken, ohne die diese Arbeit nicht möglich gewesen wäre.

Als erstes möchte ich mich bei Prof. Dr. Thomas Hebbeker bedanken, der es mir ermöglicht hat, an seinem Institut diese Arbeit zu verfassen. In den zahlreichen Meetings konnte ich eine Menge über die Arbeitsweise eines Physikers lernen und was es bedeutet, sich auf das Wesentliche zu konzentrieren.

An zweiter Stelle möchte ich mich bei Markus Lauscher bedanken, der mir beim Schreiben dieser Arbeit und in den unzählbaren Stunden während den Messungen ununterbrochen zur Seite stand. Durch seine Hilfe konnte ich eine Menge über die Programmierung in C++ und den Umgang mit Linux lernen. Deine Hilfe beim Umgang mit SiPMs und der Elektronik war Gold wert und ich wüsste nicht, wie diese Arbeit ohne dich zustande gekommen wäre. Natürlich möchte ich mich auch dafür bedanken, dass du dir die Zeit genommen hast, diese Arbeit Korrektur zu lesen. Zudem gab es so viele weitere, kleinere und größere Probleme bei denen du mir geholfen hast, wofür ich mich bei dir nochmals bedanken möchte!

Weiter möchte ich mich bei meinen Freunden und Kollegen Simon Nieswand und Sebastian Mann bedanken. Die netten und teilweise auch sinnvollen Gespräche im Büro haben die Zeit während des Programmierens und Schreibens sehr viel lustiger und entspannter gemacht.

Zudem möchte ich Tim Niggemann danken, dass er sich die Zeit genommen hat, mir beim Einstieg in Python und bei der Einrichtung von Eclipse zu helfen. Dies gilt besonders auch für Maurice Stephan und Dr. Markus Merschmeyer, die mir mit ihrem Wissen über SiPMs und ihren Ratschlägen zur Seite standen.

Ein großes Dankeschön geht auch an die Teilnehmer der Dienstags- und Mittwochsmeetings, die mir mit ihren Hilfestellungen helfen konnten diese Arbeit zu verfassen. Für die nette Arbeitsatmosphäre und die vielen Unterhaltungen möchte ich mich zudem bei allen anderen auf unserem Flur bedanken.

Weiter möchte ich meinen Freunden danken, die mir während dieser Arbeit immer wieder geraten haben, mich doch lieber mit den schönen Dingen des Lebens zu beschäftigen und die mir dadurch die nötige Abwechslung gegeben haben.

Zu guter Letzt möchte ich mich bei meiner Familie für die schönen Essen jeden Sonntag bedanken. Ein besonderer Dank geht hier an meine liebe Lisa Gatzweiler, mit der ich in dieser Zeit leider viel zu wenig Zeit verbringen konnte. Egal wie verzweifelt ich war, du hast mich jedes Mal durch deine einzigartige Art aufgemuntert und mich zum Lachen gebracht. Danke.

Erklärung

Hiermit versichere ich, dass ich diese Arbeit einschließlich beigefügter Zeichnungen, Darstellungen und Tabellen selbstständig angefertigt und keine anderen als die angegebenen Hilfsmittel und Quellen verwendet habe. Alle Stellen, die dem Wortlaut oder dem Sinn nach anderen Werken entnommen sind, habe ich in jedem einzelnen Fall unter genauer Angabe der Quelle deutlich als Entlehnung kenntlich gemacht.

Aachen, den 18. September 2012

Daniel Wilson